





RESEARCH ARTICLE | SEPTEMBER 19 2023

## Coexistence of stationary Görtler and crossflow instabilities in boundary layers

Ken Chun Kit Uy (黃駿傑) ; Jiaao Hao (郝佳傲)  ; Chih-Yung Wen (溫志湧) 



*Physics of Fluids* 35, 094115 (2023)

<https://doi.org/10.1063/5.0160098>



### Articles You May Be Interested In

Secondary instability of stationary Görtler vortices originating from first/second Mack mode

*Physics of Fluids* (March 2020)

Effect of multiple Görtler vortices on roughness-induced transition in a high-speed boundary layer

*Physics of Fluids* (July 2024)

Identification of traveling crossflow waves under real hypersonic flight conditions

*Physics of Fluids* (April 2021)



Physics of Fluids

Special Topics Open  
for Submissions

[Learn More](#)

# Coexistence of stationary Görtler and crossflow instabilities in boundary layers

Cite as: Phys. Fluids **35**, 094115 (2023); doi: [10.1063/5.0160098](https://doi.org/10.1063/5.0160098)

Submitted: 30 May 2023 · Accepted: 31 August 2023 ·

Published Online: 19 September 2023



View Online



Export Citation



CrossMark

Ken Chun Kit Uy (黃駿傑), Jiaao Hao (郝佳傲), <sup>a)</sup> and Chih-Yung Wen (溫志湧)

## AFFILIATIONS

Department of Aeronautical and Aviation Engineering, The Hong Kong Polytechnic University, Hung Hom, Kowloon, Hong Kong

<sup>a)</sup> Author to whom correspondence should be addressed: [jiaao.hao@polyu.edu.hk](mailto:jiaao.hao@polyu.edu.hk)

## ABSTRACT

The coexistence of stationary Görtler and crossflow instabilities in boundary layers covering incompressible to hypersonic regimes is investigated by varying the local sweep angle, pressure gradient, wall curvature, and wall temperature using linear stability analysis. The results show that increasing the local sweep angle under a fixed concave curvature in incompressible boundary layers leads to the appearance of two unstable modes at certain sweep angles, which is conventionally known as the “changeover” regime between the crossflow and Görtler modes. This study identifies a synchronization between the two modes under this condition, which is similar to multiple Görtler modes and thus referred to as Görtler–crossflow modes. Three scenarios are presented to describe the possible development of these modal instabilities. In addition, increasing the concave curvature destabilizes the instability, while introducing a pressure gradient stabilizes the instability and results in a shrinkage of the unstable band of the spanwise wavenumber, as reported in the literature. In supersonic and hypersonic boundary layers, synchronization can occur near specific sweep angles and under cold wall conditions in supersonic boundary layers. As Mach number increases, the synchronization regime shifts toward lower sweep angles and wall temperature, in which the former reflects a decline in crossflow strength relative to Görtler instability, while the latter indicates the influence of thermal effects on synchronization. In hypersonic boundary layers, the crossflow instability is insignificant compared with the Görtler instability. No synchronization is identified under various parameter changes, and the first Görtler–crossflow mode dominates across the entire spanwise wavenumber ranges.

Published under an exclusive license by AIP Publishing. <https://doi.org/10.1063/5.0160098>

## I. INTRODUCTION

In the context of boundary layer transition, crossflow (CF) and Görtler (G) instabilities have been investigated separately for decades, subject to different geometric formulations.<sup>1–4</sup> Crossflow instability arises in the three-dimensional (3D) boundary layers on swept bodies, manifested as streamwise corotating vortices. Both the sweep angle and pressure gradient contribute to the generation of crossflow instability,<sup>5–9</sup> and the flow streamline is highly curved near the leading-edge region if these parameters are nonzero. A crossflow component along the curved streamline is developed,<sup>7</sup> with the maximum crossflow velocity typically reaching 3% of the streamwise velocity at the boundary layer edge, as observed in wind tunnel and flight tests.<sup>6,10</sup> On the other hand, Görtler instability is observed in boundary layers over concave surfaces in the form of streamwise counterrotating vortices, arising from the imbalance between the wall-normal pressure gradient and the centrifugal forces. However, in certain flows, such as the laminar flow control (LFC) design of supercritical wings, which have concave regions on their surfaces under sweep conditions, or the hypersonic flow engine inlet, where concave structure and

three-dimensionality are common, both crossflow and Görtler instability may coexist.<sup>11</sup> Given these scenarios, further investigation is required to determine which of these two vortex instabilities is more important, particularly in compressible boundary layer regimes.

In incompressible flow regimes, both theoretical and experimental works on the effect of crossflow on Görtler vortices have been extensively investigated. In terms of experiments, Kobayashi and Izumi<sup>12</sup> utilized hot-wire anemometry to examine the transition on a cone surface around the axis of symmetry with constant angular speed in still fluid. Five cones of varying angles were used. The experiment revealed that increasing the cone-half angle beyond 30° results in a change from pairs of counterrotating Görtler vortices to corotating crossflow vortices in flow visualization. Kohama<sup>13</sup> observed a similar transformation when studying the flow structure of a supercritical LFC wing (NASA#998A) with a concave–convex structure at the leading edge region, with the sweep angle increasing from 0° to 47°. Bippes<sup>14</sup> experimentally investigated the transition process on a cylindrical wing with concave and convex profile segments and discovered that early nonlinear development occurs on the former segments,

unlike the process with pure crossflow instability. The “changeover” from the Görtler vortex to the crossflow vortex or vice versa has thus been identified.

In addition, theoretical and numerical efforts have been dedicated to these problems. Hall<sup>15</sup> studied a flow over an infinitely long swept cylinder using asymptotic analysis and concluded that the Görtler vortices are stabilized by the crossflow and eventually disappear under large sweep angles. Collier and Malik<sup>16</sup> addressed the transformation of the Görtler instability to crossflow instability with increasing sweep angle based on the Orr–Sommerfeld approach and compared it with Kohama’s work.<sup>13</sup> Their results demonstrated that the concave surface curvature destabilizes the crossflow instability. Bassom and Hall<sup>17</sup> further investigated the relationship between Görtler and crossflow vortices based on an incompressible Falkner–Skan–Cooke (FSC) profile, finding that Görtler vortices do not exist at swept wing angles exceeding  $20^\circ$ . The incompressible FSC flow<sup>18</sup> was frequently adopted in related analyses, such as the works of Blackaby and Choudhari,<sup>19</sup> Itoh,<sup>20</sup> Otto and Denier,<sup>21</sup> Zurigat and Malik,<sup>11</sup> and Le Cunff and Zebib.<sup>22</sup> Local curvature with a quasiparallel flow assumption was assumed in the local stability analysis or parabolized stability equations (PSE) on Görtler instability, while this approximation is applicable at a large Görtler number.<sup>23</sup> In particular, Zurigat and Malik<sup>11</sup> conducted a parametric study using viscous analysis on sweep angle, pressure gradient, and wall curvature parameters, indicating that the transition from Görtler to crossflow instabilities depends on these three parameters. In other words, the Görtler instability may still exist at a large sweep angle, provided that the pressure gradient is sufficiently small. The changeover from Görtler to crossflow instability is described by the crossflow Reynolds number. More recently, Groot *et al.*<sup>24</sup> investigated the linear stability mechanism on the bottom surfaces of an X207.LS airfoil computed from a boundary layer solver and revealed that the Görtler instability dominates at a  $0^\circ$  sweep angle, while the crossflow instability emerges if the sweep angle exceeds  $20^\circ$ .

Although the impact of crossflow on Görtler instability in incompressible flow regimes has been explored in previous literature, limited

work has been conducted in compressible flow regimes. Furthermore, there is a scenario wherein both crossflow and Görtler instabilities are activated and manifested as two spatial growth rate peaks in stability analysis [e.g., Fig. 1(d) in the work of Zurigat and Malik<sup>11</sup>]; however, no further explanation of this unique condition has been given. This paper conducts a parametric study on the variation in stationary crossflow and Görtler instabilities based on the individual changes in local sweep angle  $\Lambda$ , pressure gradient  $m$  (for incompressible boundary layers only), wall curvature  $\kappa = -1/R$  ( $R$ : radius of curvature) and wall temperature (for compressible boundary layers only) under various Mach number regimes (i.e.,  $M = 0.0001, 1.5, 3.0, 4.5, 6.0, 8.0$ , and  $10.0$ ). Figure 1 shows 3D sketches of the velocity profile in a boundary layer with crossflow and curvature. A compressible Falkner–Skan–Cooke (FSC) base flow with local self-similarity is adopted, which has been recently proposed and utilized by Liu<sup>25–27</sup> in studying crossflow instability over a flat plate. This generalized FSC profile can be reduced to a two-dimensional (2D) Blasius profile (with zero curvature and sweep angle) and an incompressible FSC profile ( $M = 0.0001$ ) under specific conditions, making it highly appropriate for the current study. Linear stability analysis (LST) is employed with the given base flow input. In this study, it is assumed that the radius of curvature is much greater than the boundary layer thickness, and thus including the local curvature term in perturbation equations (in LST) is sufficient to study the Görtler instability.

It is worth noting that the crossflow and Görtler instabilities can be manifested in either stationary or traveling forms (with oscillating frequency). However, the possible presence of the first Mack modal instability (or the Tollmien–Schlichting T-S mode) under such conditions adds further complexity to the analysis. Therefore, this study focuses on elucidating the coexistence of the stationary modes first, which is fundamental in the future investigation involving the traveling disturbances.

## II. PROBLEM FORMULATION

A 3D boundary-layer flow over a concave surface with constant curvature  $\kappa$  is considered (Fig. 1). A Cartesian coordinate system with

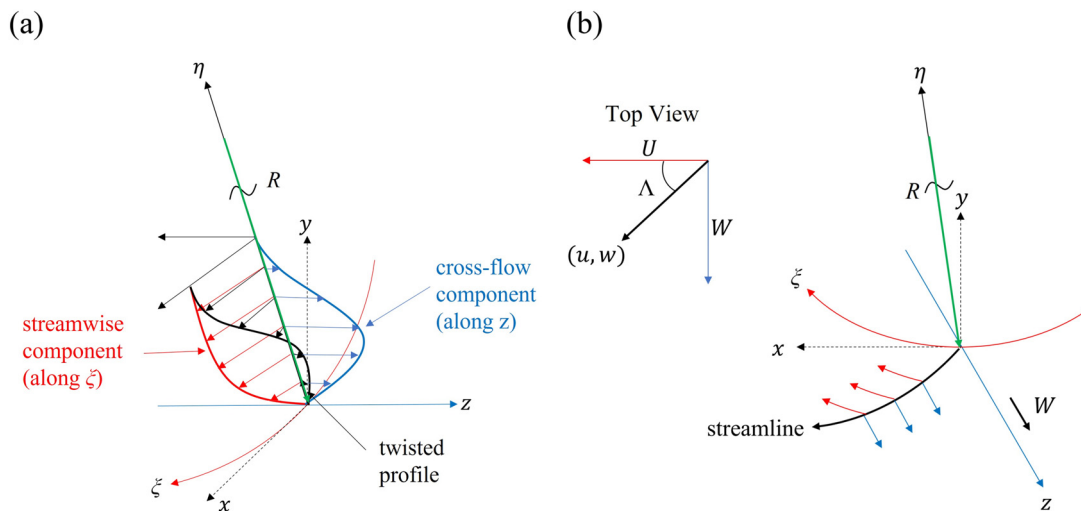


**FIG. 1.** 3D sketches of the velocity profile in a boundary layer subjected to crossflow and curvature. Two perspectives are shown: (a) with the  $x$  axis out of the plane and (b) with the  $z$  axis out of the plane, along with a top view.

$x$ -,  $y$ -, and  $z$ -directions is established. Additionally, a curvilinear coordinate system is defined, where  $\xi$  is the distance along the curved surface and  $\eta$  is the wall-normal distance from the curved surface. The two coordinates share the same  $z$ -direction.

The baseline flow condition for this study is based on a typical case adopted in Ma and Zhong's work,<sup>28</sup> and the relevant parameters are summarized in Table I (i.e., boundary layer edge Mach number  $M_e$ , unit Reynolds number  $Re_e$  and boundary layer edge temperature  $T_e$ ). The study assumes an adiabatic wall condition (subscript ad) unless otherwise specified. The characteristic length  $L$  is fixed at 0.28 mm such that the local Reynolds number  $Re = Re_e L = 2000$ . Three normalized wall curvatures are tested in this study:  $\kappa = 0$  (no curvature),  $-0.00028$  and  $-0.00056$ . For ease of reference in the remaining sections, the latter two values are labeled as  $-\kappa_L$  and  $-2\kappa_L$ , respectively, where  $\kappa_L = 0.00028$ . The corresponding Görtler numbers  $Gn \equiv Re \sqrt{\delta_x/R}$  are 0, 33, and 47, respectively, where  $\delta_x = \sqrt{x/Re_\infty}$ . The latter two  $Gn$  are sufficiently large for local stability analysis.<sup>23</sup>

### A. Model base flow

In this study, a compressible FSC profile is utilized under a local sweep.<sup>25–27</sup> This model flow is governed by the boundary layer equations. A constant pressure gradient  $m$  is introduced such that the Falkner–Skan velocity distribution is satisfied as follows:

$$U_e(\xi_{FSC}) = C \xi_{FSC}^m, \quad (1)$$

where  $U_e$  is the transformed velocity component along the  $\xi$ -direction at the edge of the boundary layer (subscript  $e$ ),  $\xi_{FSC}$  is the transformed  $\xi$  in the FSC profile and  $C$  is a constant. A positive  $m$  indicates a favorable pressure gradient, while a negative  $m$  indicates an adverse pressure gradient.

Under the local similarity assumption, the transformed boundary layer equations can be reduced to an ordinary differential equation (ODE) system with  $f' = U/U_e$ ,  $g = W/W_e$  and  $\tau = T/T_e$  representing the normalized  $\xi$ -direction velocity,  $z$ -direction velocity and temperature in the transformed FSC solution, respectively, and are expressed as follows:

$$(Nf'')' + ff'' = \frac{2m}{(m+1)S} (f'^2 - \tau), \quad (2)$$

$$(Ng')' + fg' = 0, \quad (3)$$

$$\left(\frac{N}{Pr}\tau'\right)' + (S-1)(N(f'^2))' + (K-1)S(N(g^2))' + f\left(\tau' + (S-1)(f'^2)' + (K-1)S(g^2)'\right) = 0, \quad (4)$$

$$\text{At } \eta_{FSC} = 0 : f = f' = g = 0, \quad \tau = \tau_w \text{ (isothermal) or } \tau' = 0 \text{ (adiabatic)}, \quad (5)$$

$$\text{At } \eta_{FSC} \rightarrow \infty : f' = g = \tau = 1. \quad (6)$$

TABLE I. Flow parameters for the baseline case.

$M_e$	$Re_e (m^{-1})$	$T_e (K)$
4.5	$7.2 \times 10^6$	65.15

The wall boundary conditions (subscript  $w$ ) would be different for  $\tau$  in the case of an isothermal wall and an adiabatic wall condition.  $\eta_{FSC}$  denotes the transformed  $\eta$  in the FSC profile.  $Pr$  is the Prandtl number, set as 0.72 in this study. The Chapman–Rubesin factor  $N$  (obtained from Sutherland's law) and parameters  $S$  and  $K$  are defined as follows:

$$N = \sqrt{\tau} \left( \frac{1 + T_s/T_e}{\tau + T_s/T_e} \right), \quad (7)$$

$$S = \left( 1 + \frac{\gamma-1}{2} M^2 \cos^2 \Lambda \right), \quad (8)$$

$$K = \left( 1 + \frac{\gamma-1}{2} M^2 \right) / S, \quad (9)$$

where  $T_s = 110.4$  K,  $\gamma = 1.4$  is the specific heat ratio, and  $S$  and  $K$  are correlated with the local sweep angle  $\Lambda$ ; more details can be found in Liu's work.<sup>25–27</sup> This ODE system is solved using Newton's iteration method. Using  $\Lambda$ , the local streamwise velocity (defined as  $u$ ) and the local crossflow velocity (defined as  $w$ ) along the streamline coordinate are expressed as follows [i.e., Fig. 1(b)]:

$$u(\eta) = f'(\eta) \cos^2 \Lambda + g(\eta) \sin^2 \Lambda, \quad (10)$$

$$w(\eta) = [g(\eta) - f'(\eta)] \cos \Lambda \sin \Lambda. \quad (11)$$

The flow variables are nondimensionalized with the corresponding edge parameters. The quantities discussed in the remaining sections are in normalized form unless otherwise specified.

The typical crossflow profiles obtained at different  $M$  regimes are shown in Fig. 2. The present FSC base flow is validated with the literature.<sup>25,26</sup>

### B. Linear stability analysis

Assuming that the Reynolds number is large and the boundary layer thickness is much smaller than the radius of curvature, the LST is constructed with the local curvature  $\kappa$ . The corresponding Lamé coefficients are  $h_1 = 1 + \kappa\eta$  and  $h_2 = h_3 = 1$ . With the local parallel flow assumption, the instantaneous flow  $\mathbf{U} = [\rho, \rho u, \rho v, \rho w, \rho e]^T$  (where  $\rho$  is the density,  $v$  is the local wall-normal velocity along  $\eta$ , and  $e$  is the total energy per unit mass) is discretized into a one-dimensional (1D) steady solution (represented by an overbar) and an unsteady perturbation (represented by a prime) as follows:

$$\mathbf{U}(\xi, \eta, z, t) = \bar{\mathbf{U}}(\eta) + \mathbf{U}'(\xi, \eta, z, t). \quad (12)$$

The governing equation of  $\mathbf{U}'$  is obtained through linearization and can be expressed in the following normal-mode form:

$$\mathbf{U}'(\xi, \eta, z, t) = \hat{\mathbf{U}}(\eta) \exp[i\alpha\xi + i\beta z - i\omega t] + \text{c.c.} \quad (13)$$

$\hat{\mathbf{U}}(\eta)$  is the eigenfunction in the wall-normal direction,  $\alpha$  is the streamwise wavenumber,  $\beta$  is the spanwise wavenumber,  $\omega$  is the angular frequency and c.c. is the complex conjugate. For spatial analysis,  $\alpha$  is considered to be complex with real (subscript  $r$ ) and imaginary parts (subscript  $i$ ). The spatial growth rate is denoted as  $-\alpha_i$ . An eigenvalue problem is formulated by substituting Eq. (13) into the linearized compressible Navier–Stokes equations with  $\mathbf{U}$ ,

$$\bar{\mathbf{A}}\hat{\mathbf{U}} = (\alpha_r + i\alpha_i)\hat{\mathbf{U}}, \quad (14)$$

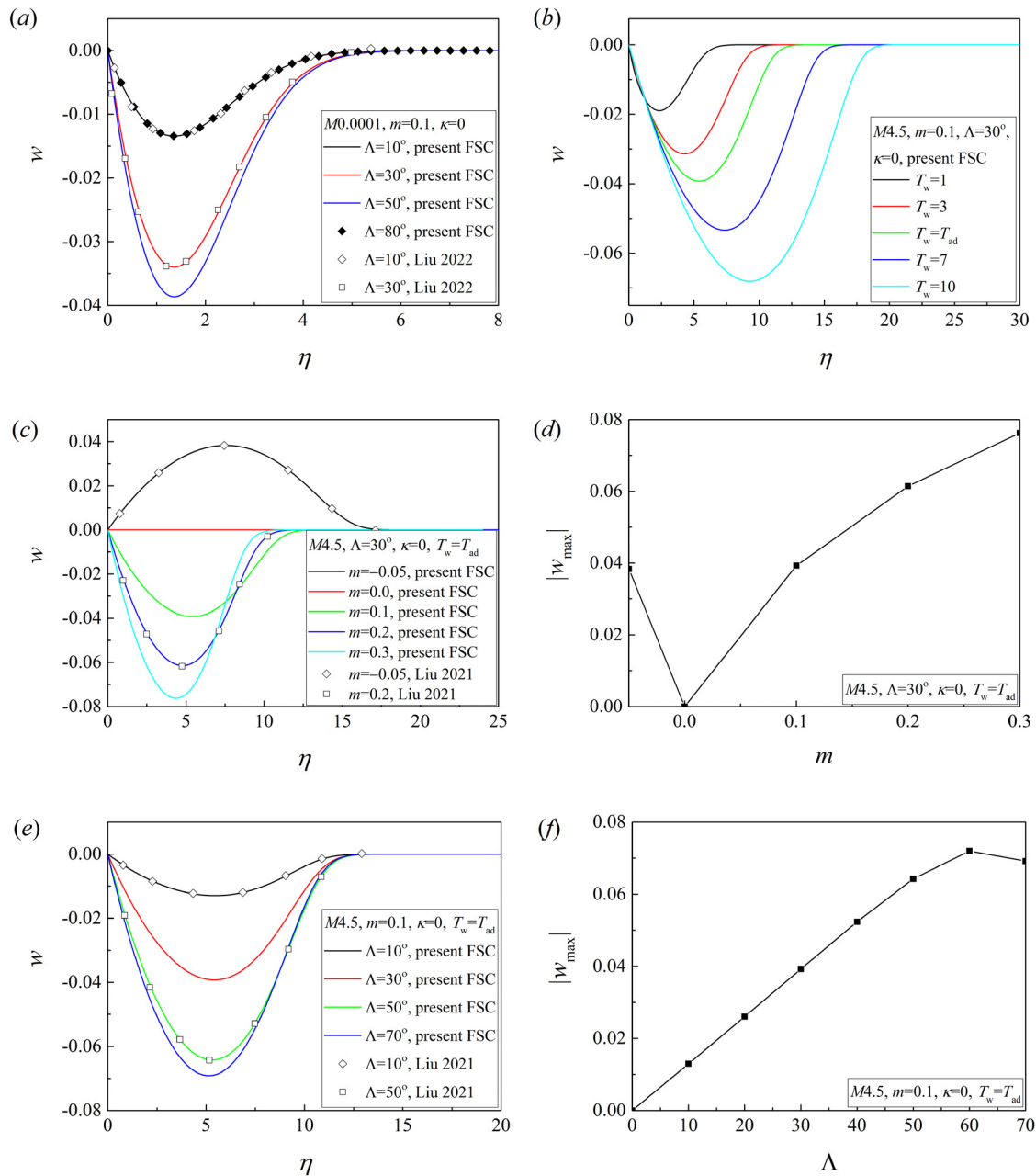


**FIG. 2.** Variation of crossflow velocity along  $\eta$  under the change of (a) local sweep angle at  $M=0.0001$ ,  $m=0.1$ , and  $\kappa=0$ , (b) wall temperature at  $M=4.5$ ,  $m=0.1$ ,  $\Lambda=30^\circ$ , and  $\kappa=0$ , (c) pressure gradient at  $M=4.5$ ,  $\Lambda=30^\circ$ ,  $\kappa=0$ , and  $T_w=T_{\text{ad}}$ , and (e) local sweep angle at  $M=4.5$ ,  $m=0.1$ ,  $\kappa=0$ , and  $T_w=T_{\text{ad}}$ . [(d) or (f)] The absolute maximum crossflow velocity  $|w_{\max}|$  for the case of (c) [or (e)]. Profiles from Liu's work<sup>25,26</sup> have been included in the figures for reference.

where  $\bar{A}$  is the Jacobian matrix composed of both the inviscid and viscous fluxes and is expressed in terms of base flow quantities. The detailed formulations can be found in the literature.<sup>29,30</sup> A C++ library Eigen<sup>31</sup> is utilized to solve the eigenvalue problem with a given  $\omega$  and  $\beta$ , and a second-order finite-difference method is used for discretization.<sup>32</sup> The boundary conditions are consistent with those in the compressible FSC profile [i.e., Eqs. (5) and (6)]. The LST solver has

been used by the authors to investigate the Görtler instability in a 2D base flow.<sup>33</sup> A comparison between the present LST result and the literature<sup>26</sup> in capturing the crossflow instability of a 3D FSC base flow is shown in Fig. 3. For constructing the FSC base flow, an algebraic mapping is employed, ensuring that at least half of the grid points are positioned within the boundary layer (more detail can be found in Malik's work<sup>32</sup>). In the context of grid converging study, two cases are



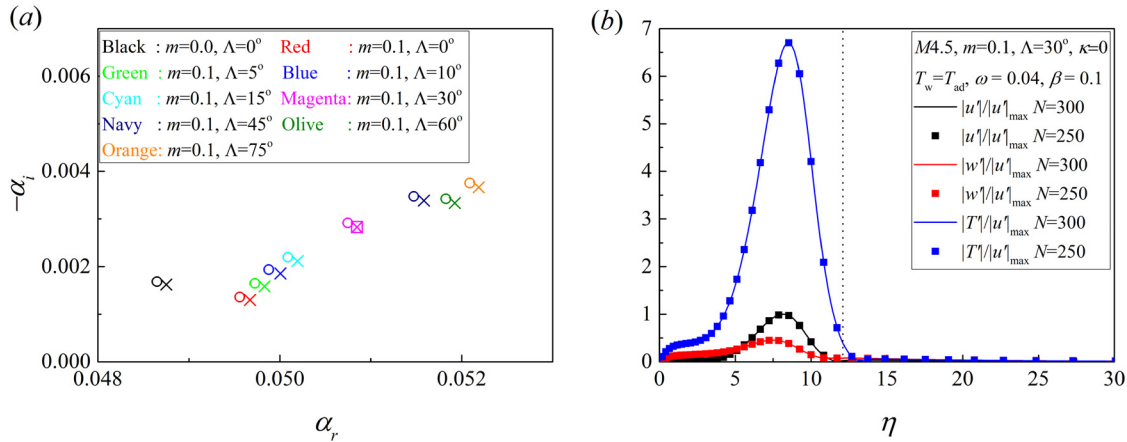


**FIG. 3.** (a) Eigenvalue spectrum of the unstable mode for different base flows.  $M=4.5$ ,  $\kappa=0$ ,  $T_w=T_{ad}$ ,  $Re=2000$ ,  $\omega=0.04$ , and  $\beta=0.1$ . Circles denote the data from literature,<sup>26</sup> crosses denote the present LST at  $N=200$ , and square denotes the present LST at  $N=300$ . (b) Grid convergence study of the disturbance profiles (i.e.,  $|u|/|u|_{\max}$ ,  $|w|/|u|_{\max}$  and  $|T|/|u|_{\max}$ ) for a selected case, i.e.,  $M=4.5$ ,  $\kappa=0$ ,  $T_w=T_{ad}$ ,  $Re=2000$ ,  $\omega=0.04$ ,  $\beta=0.1$ ,  $m=0.1$ , and  $\Lambda=30^\circ$ .

considered, with total grid points  $N=250$  and  $300$  at  $\eta$ -direction, respectively, and the corresponding eigenfunctions are presented in Fig. 3(b). Notably, the good agreement between these two cases indicates that the coarser grid with  $N=250$  is sufficient for capturing the instability, thus being adopted in the subsequent studies. Discrepancies of at most 4.5% are observed between the results obtained from the present LST solver and the literature, which can be attributed to the usage of different eigenvalue solvers or discretization method. The present LST solver has been verified.

### III. RESULTS

#### A. Incompressible boundary layers

In this part, incompressible FSC profiles are established at  $M=0.0001$  while keeping the other flow conditions ( $Re_e$  and  $T_e$ ) as specified in Table I and varying the parameters  $m$ ,  $\Lambda$ , and  $\kappa$  separately. The LST is performed with  $\omega=0$ , and the corresponding spatial maximum growth rates are presented in Fig. 4. It is known that the instability is of the crossflow type if  $\kappa=0$  and  $m$  and  $\Lambda$  are nonzero [i.e., Fig. 4(a)]. As seen, the increase in  $\Lambda$  (i.e.,  $\Lambda=10^\circ$ ,  $30^\circ$ ,  $50^\circ$ ) leads to the destabilization of crossflow instability bounded within  $\beta=1$ , which is consistent with previous literature.<sup>11,26</sup> The peak growth rate is always at  $\beta=0.35$ . In Fig. 4(b), when a concave curvature with  $\kappa=-2\kappa_L$  denoting the occurrence of Görtler instability is introduced in the system, the overall instability is different from that in Fig. 4(a), and larger  $\beta$  ranges (i.e.,  $\beta>1$ ) of instability are activated. The peak growth rate for  $\Lambda=1^\circ$  is at  $\beta=1.75$ , while for  $\Lambda=50^\circ$ , it is at  $\beta=0.45$ . In Fig. 4(c), changing the parameter  $m$  (i.e.,  $m=-0.05$ ,  $0$ ,  $0.1$ ,  $0.2$ ) leads to the dominance of crossflow instability at  $\Lambda=30^\circ$  for both positive (favorable) or negative (adverse) pressure gradients, while the instability is solely the Görtler type at  $m=0$  (absence of crossflow component). Increasing the concave wall curvature (i.e.,  $\kappa=0$ ,  $-1\kappa_L$ ,  $-2\kappa_L$ ) in Fig. 4(d) transforms the instability from crossflow to hybrid Görtler and crossflow type with the expansion of unstable  $\beta$  ranges. Regarding the effect of crossflow on Görtler instability, Zurigat and Malik<sup>11</sup> suggested that there is a changeover sweep angle [i.e.,  $\Lambda=22^\circ$  in Fig. 4(b)] in which the stability is Görtler type before this critical  $\Lambda$ ,

while the instability becomes the crossflow type beyond this critical  $\Lambda$ . In addition, the coexistence of two growth rate peaks denoting the crossflow mode [i.e., at  $\beta=0.5$  for  $\Lambda=20^\circ$  in Fig. 4(b)] and the Görtler mode [i.e., at  $\beta=1.45$  for  $\Lambda=20^\circ$  in Fig. 4(b)] are recorded near the changeover sweep angle, consistent with previous literature.<sup>11</sup>

Although the results in Fig. 4 have been reported before,<sup>11</sup> the origins of the unstable modes at the changeover regimes in Fig. 4(b) remain unclear and warrant further investigation. Figure 5 presents an eigenvalue spectrum under changes in  $\Lambda$  and  $\kappa$  at  $m=0.1$  and  $\beta=0.5$ . At  $\Lambda=0^\circ$  and  $\kappa=-2\kappa_L$ , the instability is of the Görtler type, and multiple eigenvalue modes are excited by the entropy/vorticity wave at  $\alpha_r=0$ .<sup>29,34</sup> On the other hand, at zero curvature and  $\Lambda>0^\circ$ , the instability is of the crossflow type, and only one unstable mode (with  $-\alpha_i>0$ ) is recorded, which becomes more unstable as  $\Lambda$  increases (see the red arrow). However, if both  $\Lambda$  and  $\kappa$  are nonzero, the instability exhibits multiple eigenvalue modes analogous to the Görtler instability<sup>34,35</sup> at small  $\Lambda$  (i.e.,  $\Lambda=5^\circ$ ,  $10^\circ$ ), while the modes become more stable as  $\Lambda$  increases (see the black arrow), and eventually only one unstable mode is recorded at large  $\Lambda$  (i.e.,  $\Lambda=15^\circ$ ). This suggests that the instability under the coexistence of Görtler and crossflow instabilities (or defined as Görtler-crossflow (GCF) instability) may have the same origin as the Görtler instability. The most unstable GCF mode is attenuated as  $\Lambda$  increases at a fixed concave curvature, analogous to the statement described in the literature<sup>11</sup> that the crossflow stabilizes the Görtler instability.

To further investigate the differences and similarities between the Görtler, crossflow, and GCF modes, the corresponding variation in disturbance profiles is presented. The disturbance profiles of a typical case of Görtler instability with a zero sweep angle are shown in Fig. 6. The first Görtler mode is identified as the largest eigenvalue mode, while the second Görtler mode corresponds to the second largest eigenvalue mode. The streamwise velocity disturbance profile exhibits a single peak within the boundary layer for the first Görtler mode and two peaks with an inflection point denoting the abrupt gradient changes [indicated by the corresponding square in Fig. 6(b)] for the second Görtler mode. Similarly, the spanwise velocity disturbance

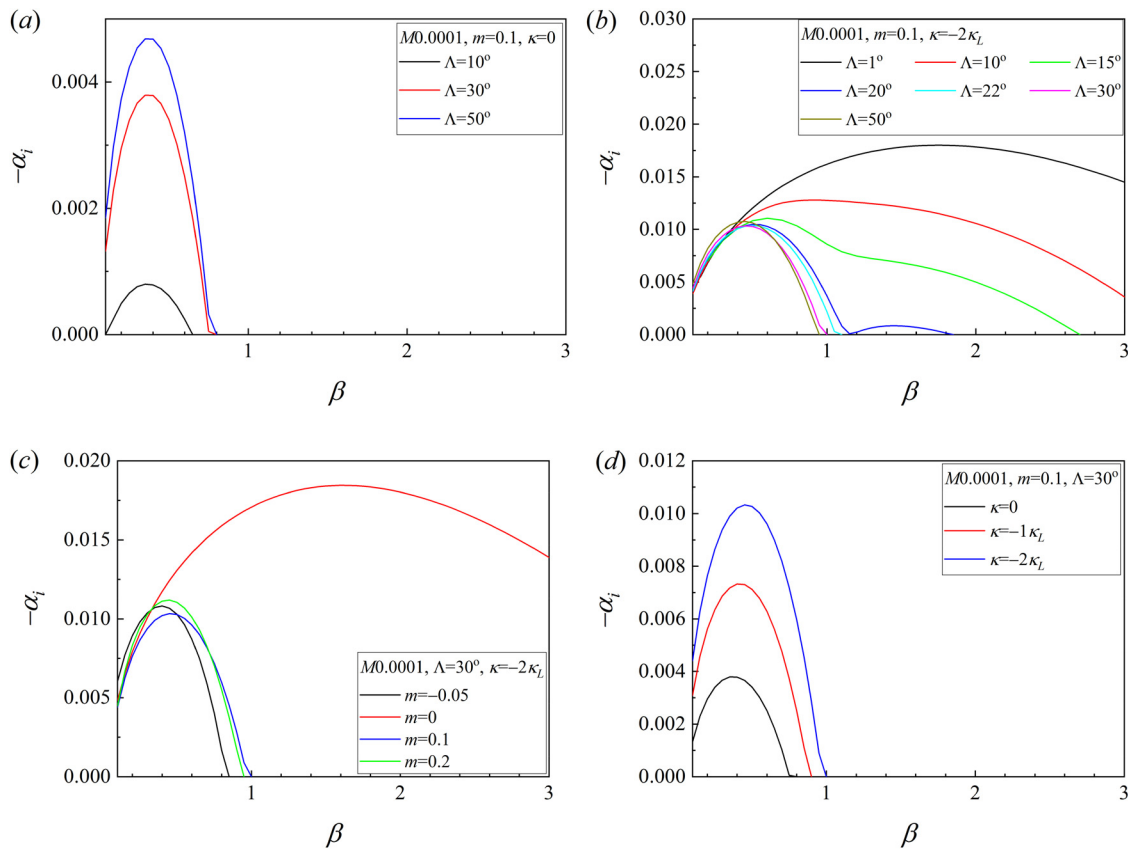


**FIG. 4.** Spatial maximum growth rate vs spanwise wavenumber at  $M=0.0001$  and  $\omega=0$  under changes in the (a) local sweep angle at  $m=0.1$  and  $\kappa=0$ , (b) local sweep angle at  $m=0.1$  and  $\kappa=-2\kappa_L$ , (c) pressure gradient at  $\Lambda=30^\circ$  and  $\kappa=-2\kappa_L$ , and (d) wall curvature at  $m=0.1$  and  $\Lambda=30^\circ$ .

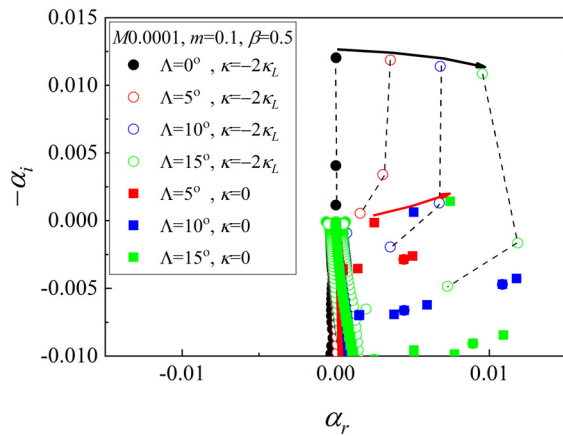


**FIG. 5.** Eigenvalue spectrum under the changes in  $\Lambda$  and  $\kappa$  at  $M=0.0001$ ,  $m=0.1$ ,  $\omega=0$ , and  $\beta=0.5$ . Dashed lines connect the three largest eigenvalue modes of the corresponding cases at  $\kappa=-2\kappa_L$ . The black arrow indicates the shift of the most unstable Görtler or GCF mode from  $\Lambda=0^\circ$  to  $15^\circ$  at  $\kappa=-2\kappa_L$ , whereas the red arrow indicates the shift of the crossflow mode from  $\Lambda=5^\circ$  to  $15^\circ$  at  $\kappa=0$ .

profile exhibits two peaks for the first Görtler mode and three peaks for the second Görtler mode. Notably, the corresponding disturbance profiles can be existed in the form of positive-negative peaks or negative-positive peaks with inflection points near the  $\eta$  axis as depicted in literature.<sup>29</sup> For the purpose of clarity, all the disturbance profiles in this study are presented in terms of absolute magnitudes. It is conventionally known that the second Görtler mode is always more stable than the first Görtler mode across the entire  $\beta$  range.<sup>35</sup> The disturbance attaches to the boundary layer wall (moves toward the wall) as  $\beta$  increases for both the first and second Görtler modes.

The variation in the disturbance profile for a typical crossflow instability is provided in Fig. 7. A single peak is recorded within the boundary layer for the streamwise velocity disturbance profile,<sup>26</sup> and the disturbance peak moves away from the wall as  $\beta$  increases. Multiple peaks are identified in the crossflow velocity disturbance [Fig. 7(b)], and these disturbances expand beyond the boundary layer edge.

The growth rate (i.e.,  $-\alpha_i$ ) and  $\alpha_r$  plotted against  $\beta$  in the change-over sweep angle region (i.e.,  $\Lambda=20^\circ$  and  $\Lambda=22^\circ$ ) at a fixed curvature are shown in Fig. 8, representing two cases of GCF instability. For the case of  $\Lambda=20^\circ$ , the first GCF mode with a local maximum (or the crossflow mode defined in Zurigat and Malik<sup>11</sup>) is always unstable at

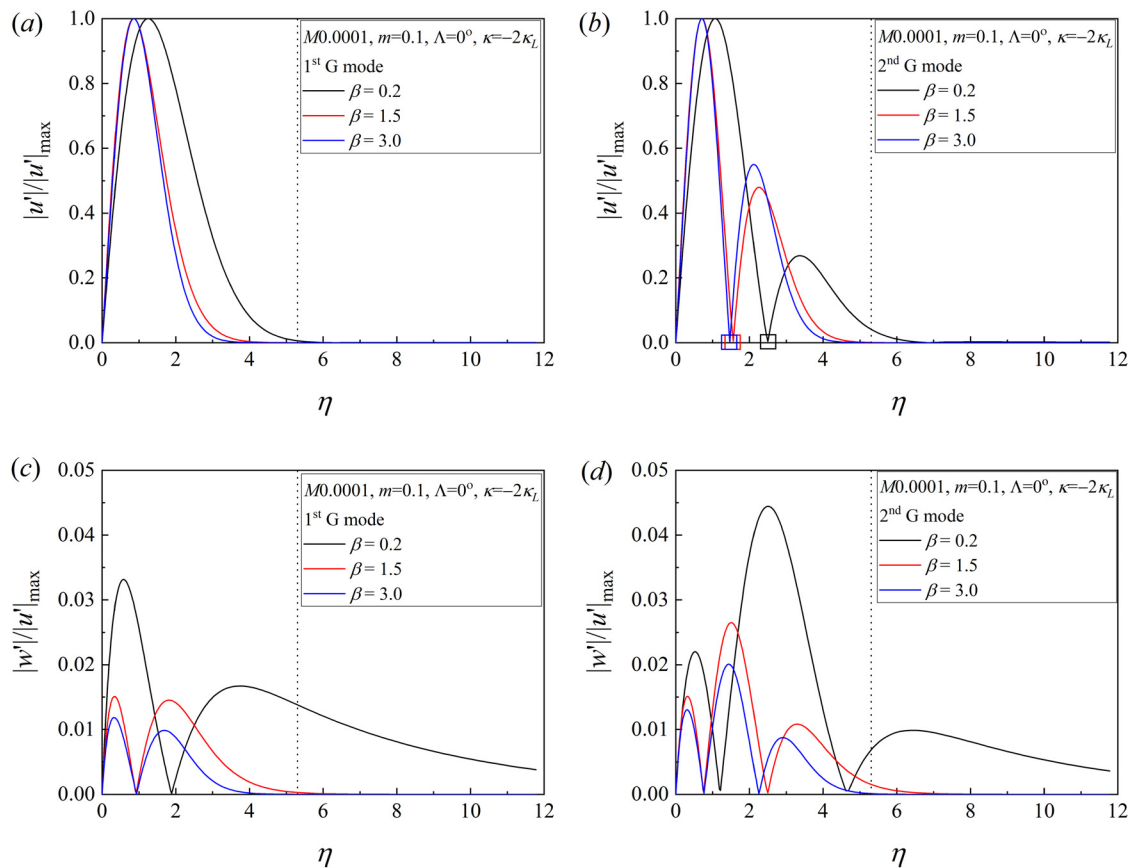


**FIG. 6.** Variation in streamwise and crossflow velocity disturbance profiles for the first Görtler mode [(a) and (c), respectively] and the second Görtler mode [(b) and (d), respectively] as  $\beta$  increases. Squares on  $\eta$  axis indicate the inflection points. The dotted line denotes the boundary layer edge.  $M = 0.0001$ ,  $m = 0.1$ ,  $\Lambda = 0^\circ$ , and  $\kappa = -2\kappa_L$ .

small  $\beta$  values [Fig. 8(c)]. As  $\beta$  increases, a possible exchange between the two eigenvalue modes is observed at approximately  $\beta = 1.145$ , accompanied by the emergence of another local maximum (or the Görtler mode defined in Zurigat and Malik<sup>11</sup>) [see Fig. 8(a)]. On the other hand, for the case of  $\Lambda = 22^\circ$ , an overlapping between the two GCF modes is found at around  $\beta = 1.19$ , and one mode is slightly destabilized. However, its growth rate  $\alpha_i$  remains positive throughout the range of  $\beta$  and is therefore considered stable.

Referring to the previous study on the Mack modal instabilities by Ma and Zhong,<sup>28</sup> it is postulated that the above-mentioned mode exchange process is a result of synchronization phenomena. To clarify this synchronization process, the first (or second) GCF mode is defined accordingly when the modal instability consists of no (or single) inflection point on the streamwise velocity disturbance profile at small  $\beta$  [shown in Figs. 10(a) and 10(b), i.e., with an inflection point (indicated by a square) recorded at around  $\eta = 2$  for the second GCF mode at  $\beta = 0.2$ ]. The occurrence of synchronization is verified by examining the streamwise and crossflow velocity disturbance profiles at the indicated  $\beta$  values for the two  $\Lambda$  cases (Fig. 9). At  $\Lambda = 20^\circ$ , the striking resemblance between the two GCF disturbance profiles and the negligible difference in  $\alpha_r$  at  $\beta = 1.145$  [i.e., 0.05% as evaluated

from the inset of Fig. 8(c)] for the two eigenmodes strongly suggest the presence of synchronization, which aligns with the findings in Ma and Zhong's work.<sup>28</sup> Meanwhile, at  $\Lambda = 22^\circ$ , the two disturbance profiles exhibit similarity, implying a possible occurrence of synchronization. However, a comparatively larger  $\alpha_r$  difference between the two eigenmodes [i.e., around 6%, as evaluated from the inset of Fig. 8(d)] indicates the absence of synchronization at this  $\Lambda$ . The changeover regimes identified in previous work<sup>11</sup> actually pinpoint the critical sweep angle near the synchronization regime, at which the first GCF mode is destabilized or stabilized, while the second GCF mode behaves in the opposite manner.

Based on the analysis in Fig. 5, the similarities between the first two GCF modes (i.e., Fig. 10) and the first two Görtler modes (i.e., Fig. 6) are compared and identified. For the first GCF mode, the crossflow velocity disturbance moves away from the wall as  $\beta$  increases [Fig. 10(c)], while the disturbance moves toward the wall for the second GCF mode [Fig. 10(d)]. The analysis of the disturbance propagating direction (i.e., moving toward/away from wall) in the GCF modes indicates that a mode exchange between the two GCF modes occurs after  $\beta = 1.145$  for  $\Lambda = 20^\circ$  [illustrated in the inset of Fig. 8(b)], in which the most unstable mode changes from the first GCF mode to



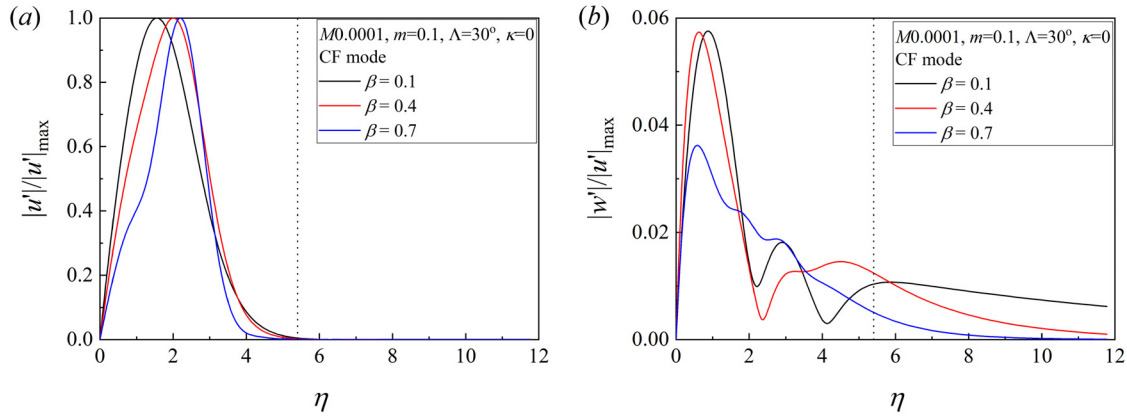


**FIG. 7.** Variation in the (a) streamwise velocity and (b) crossflow velocity disturbance profile for the crossflow mode as  $\beta$  increases. The dotted line denotes the boundary layer edge.  $M = 0.0001$ ,  $m = 0.1$ ,  $\Lambda = 30^\circ$ , and  $\kappa = 0$ .

the second GCF mode. This is regarded as a characteristic feature after the synchronization as stated in the previous study.<sup>28</sup> This differs from the case of Görtler instability, in which the disturbances in both the first and second Görtler modes move toward the

wall. Therefore, it is postulated that the introduction of crossflow instability to the Görtler instability changes the nature of the first Görtler mode, and synchronization between the modes may exist. In addition, unlike the behavior of the second Görtler modes

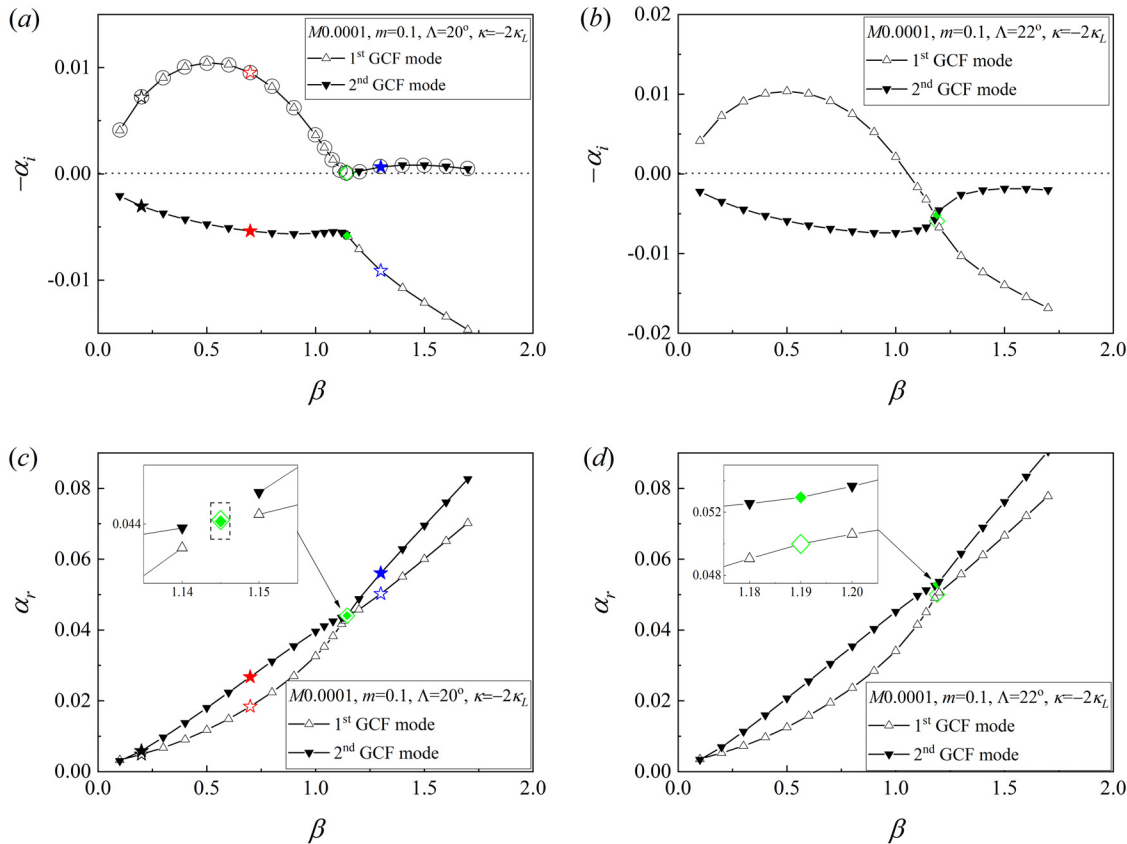


**FIG. 8.** Growth rate (or  $\alpha_r$ ) vs  $\beta$  for cases of (a) [or (c)]  $\Lambda = 20^\circ$  and (b) [or (d)]  $\Lambda = 22^\circ$  at  $M = 0.0001$ ,  $m = 0.1$ , and  $\kappa = -2\kappa_L$ . Circles represent the largest unstable modes at the corresponding  $\beta$ . The star icons in (a) and (c) indicate  $\beta = 0.2$  (black),  $0.7$  (red), and  $1.3$  (blue), and the green rhombus icons in (a)–(d) indicate the corresponding eigenmodes in Fig. 9. Dash line square in the inset of Fig. 8(c) denotes the regime for possible mode exchanges.

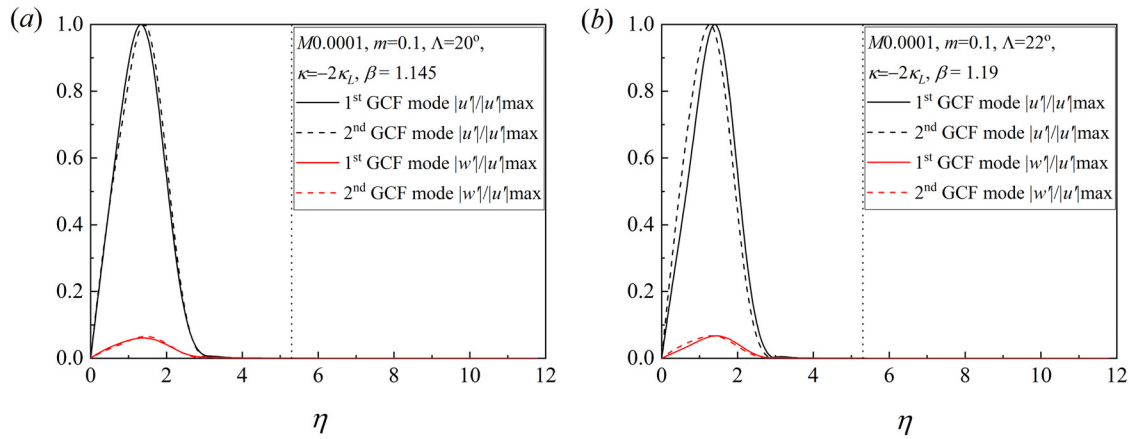


**FIG. 9.** Variation in the streamwise velocity and crossflow velocity disturbance profiles for the corresponding eigenmodes indicated in (a) the inset of Figs. 8(c) and 8(b) the inset of Fig. 8(d). The dotted line denotes the boundary layer edge.

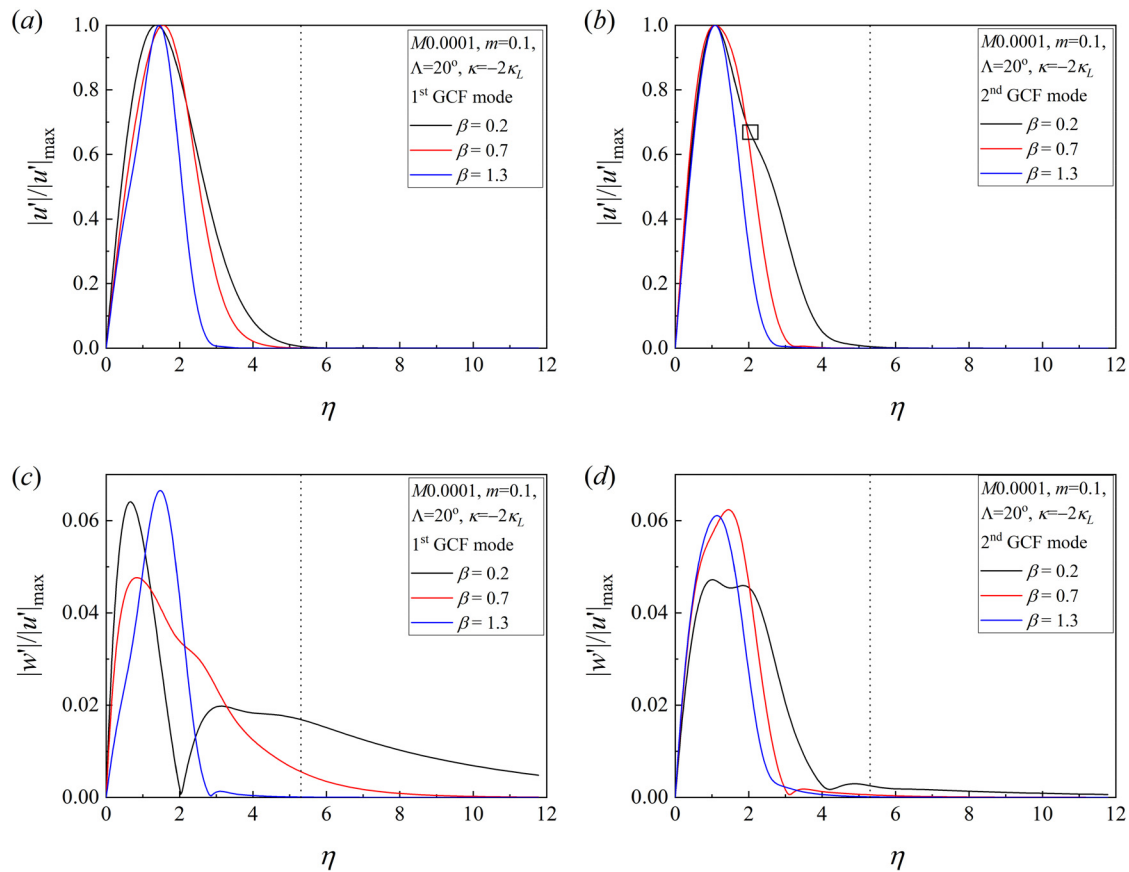


**FIG. 10.** Variation in the streamwise velocity and crossflow velocity disturbance profiles for the first [(a) and (c), respectively] and the second [(b) and (d), respectively] GCF modes as  $\beta$  increases. Square indicates the inflection point. The dotted line denotes the boundary layer edge.  $M = 0.0001$ ,  $m = 0.1$ ,  $\Lambda = 20^\circ$ , and  $\kappa = -2\kappa_L$ .

described in the literature,<sup>35</sup> the second GCF mode may take on the dominant role of instability over the first GCF mode as  $\beta$  increases near the changeover sweep angle region [Fig. 8(a)]. Limited similarity between the GCF and crossflow modes is identified by comparison with the crossflow velocity disturbance profiles in Fig. 7 (crossflow instability) and Fig. 10 (GCF instability).

Drawing on insights from previous studies on Mack modal instabilities and the current LST results, three criteria for identifying the synchronization regime between the GCF modes are outlined as below: (1) the differences in  $\alpha_r$  between the two eigenmodes should be sufficiently small; (2) the disturbance profiles (or mode shape structure) of the two eigenmodes should exhibit significant similarity; and (3) after the synchronization regime, mode exchanges can be identified by analyzing the disturbance propagating directions of the two eigenmodes as  $\beta$  increases. These criteria will be applied in the subsequent stability analysis.

In conclusion, evidence of synchronization occurring in the vicinity of the changeover regime is provided in the incompressible boundary layer. The modal instabilities observed at the changeover regime, referred to as the GCF instability, have been compared with the well-known crossflow and Görtler modes. The GCF instability exhibits characteristics that resemble multiple Görtler modes, suggesting that these combined modes may originate from the Görtler instability. Consequently, the previous literature's description of the transition from crossflow to Görtler modes at the changeover regime<sup>11</sup> may not be entirely accurate. To provide a more appropriate representation, the term “mode exchange” regime is defined instead to characterize the phenomenon of mode exchange from the first GCF mode to the second GCF mode, typically observed after synchronization occurs.

## B. Supersonic boundary layers ( $M$ 1.5–4.5)

The supersonic boundary layers (i.e.,  $M = 1.5, 3.0$ , and  $4.5$ ) are examined under changes in  $\Lambda$ ,  $\kappa$ , and  $T_w$ . It is important to note that the value of  $|w_{\max}|$  plays a crucial role in determining the characteristics of crossflow instability. The individual impacts of increasing  $m$  and  $\Lambda$  on the crossflow instability exhibit similarity [as shown in Figs. 2(d) and 2(f)], with the following conditions excluded: (1)  $m \leq 0$  and (2)  $\Lambda \geq \Lambda_p$  [where  $\Lambda_p$  denotes the corresponding sweep angle at which

the peak value of  $|w_{\max}|$  is attained, as defined in Liu's work.<sup>25</sup> For example,  $\Lambda_p$  is at  $60^\circ$  in Fig. 2(f)]. In view of this, the parameter  $m$  is fixed in the subsequent studies to avoid the redundancy, while the influence of  $\Lambda$  is demonstrated.

The impact of  $\Lambda$ ,  $\kappa$ , and  $T_w$  on the GCF instability for the  $M = 1.5$  cases are illustrated in Fig. 11. Under a fixed curvature, the first Görtler/GCF mode, covering larger  $\beta$  ranges ( $\beta = 0.1$ – $3.0$ ), dominates at small  $\Lambda$ , while synchronization occurs at  $\Lambda = 16^\circ$  with the emergence of two local maximum. Above (or below) this angle, the first GCF mode dominates within smaller  $\beta$  ranges (i.e.,  $\beta < 1$ ) before synchronization, and the second GCF mode becomes stable (or unstable) after synchronization at  $\beta > 1$ . The peak growth rate for  $\Lambda = 1^\circ$  is at  $\beta = 1.25$ , while for  $\Lambda = 50^\circ$ , it is at  $\beta = 0.35$ . A decrease in  $\kappa$  (corresponding to an increase in concave curvature) enhances the modal instability [i.e., Fig. 11(b)], displaying a behavior akin to the local curvature effect on Görtler instability, as reported in previous work.<sup>33</sup> Additionally, the effect of cold wall temperature destabilizes the instability at first with a shift of local maximum to larger  $\beta$  value, and a synchronization may potentially occur at  $T_w = 0.7$ , indicated by the presence of an inflection point on the curve [i.e., Fig. 11(c)]. Further decrease in  $T_w$  (i.e.,  $T_w = 0.5$ ) marginally stabilized the first local maximum (at around  $\beta = 0.6$ ) while the mode is destabilized as  $\beta$  increases. A decrease in  $|w_{\max}|$  (and thus the crossflow strength) is observed at cold wall side [also evident in the  $M = 4.5$  case, as shown in Fig. 2(b)], while boundary layer thickness is thinner at wall cooling, consistent with previous literature.<sup>36</sup> Larger unstable  $\beta$  ranges are observed under cold wall conditions or at walls with more concave curvature. Notably, destabilization of Görtler instability due to wall cooling has been reported by literature<sup>33,37</sup> before, while the crossflow instability is stabilized conversely.<sup>25,38</sup> Overall, the destabilization of GCF modes underlines the significant manifestation of Görtler instability characteristics in wall cooling scenarios.

The growth rate (i.e.,  $-\alpha_i$ ) and  $\alpha_r$  vs  $\beta$  at the synchronization (i.e.,  $M = 1.5$ ,  $m = 0.1$ ,  $\Lambda = 16^\circ$ ,  $\kappa = -2\kappa_L$  and  $T_w = T_{ad}$ ) are shown in Figs. 12(a) and 12(b). In this scenario, the first GCF mode is dominant at  $\beta < 0.786$ , while the second GCF mode rises and becomes the most unstable mode at  $\beta > 0.786$ . As seen in Fig. 12(c), the disturbance profiles for the two eigenmodes at  $\beta = 0.786$  [marked in the inset of Fig. 12(b)] exhibit close similarities, while the difference in  $\alpha_r$  values

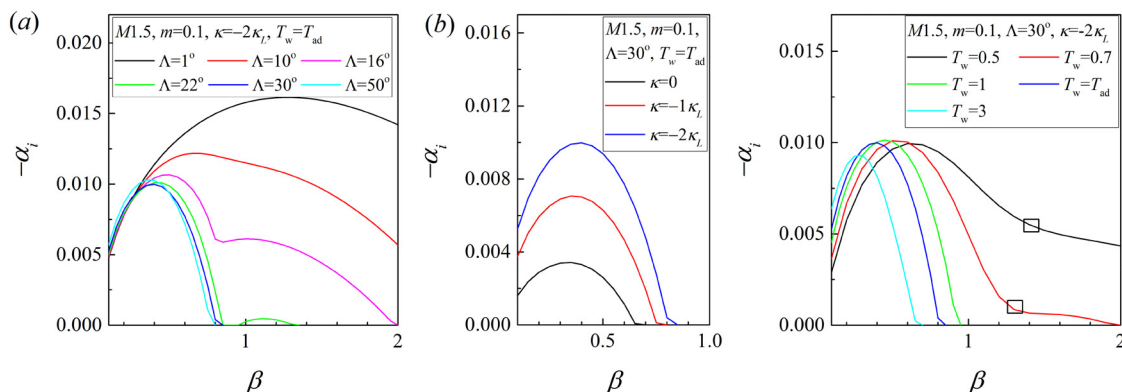


**FIG. 11.** Spatial maximum growth rate vs spanwise wavenumber at  $M = 1.5$  and  $\omega = 0$  with the change in (a) local sweep angle at  $m = 0.1$ ,  $\kappa = -2\kappa_L$ , and  $T_w = T_{ad}$ , (b) wall curvature at  $m = 0.1$ ,  $\Lambda = 30^\circ$ , and  $T_w = T_{ad}$ , and (c) wall temperature at  $m = 0.1$ ,  $\Lambda = 30^\circ$ , and  $\kappa = -2\kappa_L$ . Squares in (c) indicate inflection points.

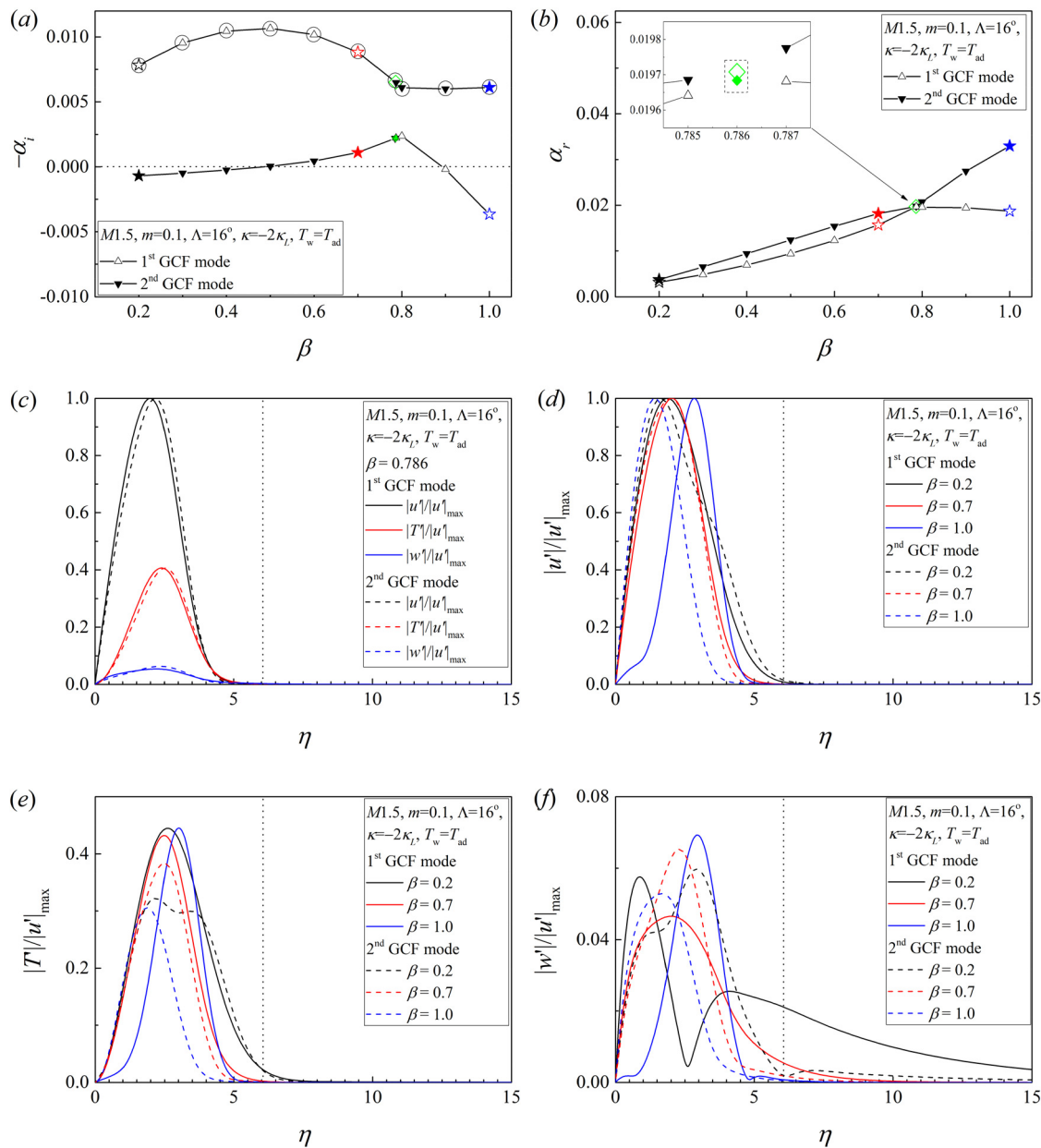


**FIG. 12.** (a) Growth rate vs  $\beta$  and (b)  $\alpha_r$  vs  $\beta$  for a case of  $M=1.5$ ,  $m=0.1$ ,  $\Lambda=16^\circ$ ,  $\kappa=-2\kappa_L$ , and  $T_w=T_{ad}$ . The star icons in (a) and (b) indicate  $\beta=0.2$  (black),  $0.7$  (red), and  $1.0$  (blue), and the green rhombus icons in (a) and (b) indicate the corresponding eigenmodes in (c). Dash line square in the inset of (b) denotes the regime for possible mode exchanges. (c) The corresponding disturbance profiles labeled by rhombus icons. The corresponding (d) streamwise velocity, (e) temperature, and (f) crossflow velocity disturbance profiles labeled by star icons. In (c)–(f), the dotted line represents the boundary layer edge.

between the two eigenmodes is remarkably small (i.e., approximately 0.12%). In addition, shifts of the corresponding streamwise velocity, temperature, and crossflow velocity disturbance to the side of the boundary layer edge (or wall) in Figs. 12(d)–12(f) are observed for the first (or second) GCF mode as  $\beta$  increases, similar to the incompressible boundary layer case (Fig. 10). These observations support the notion of a mode exchange occurring after the synchronization at

$\beta=0.786$ . Another synchronization between a higher GCF mode and the first GCF mode is identified at  $\beta > 1.0$ ; however, those modes remain stable and are not further discussed in this study. The criteria defined in Sec. III A are satisfied in this case, confirming the existence of synchronization at  $\Lambda=16^\circ$  for these flow conditions.

In Figs. 13(a) and 13(b), the real and imaginary eigenvalues of the first two GCF modes are plotted against  $\beta$  for  $T_w=0.7$  case.

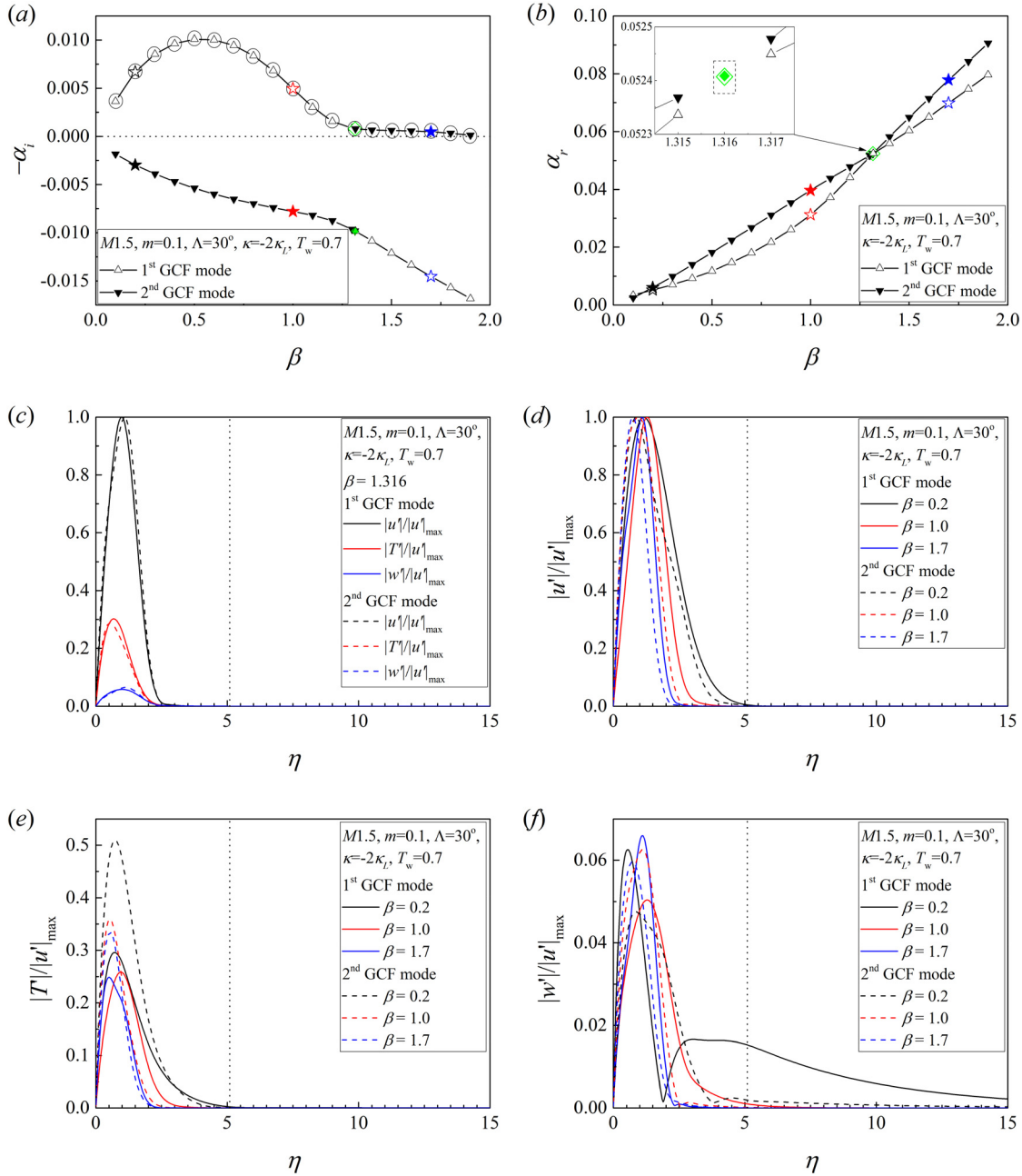


**FIG. 13.** (a) Growth rate vs  $\beta$  and (b)  $\alpha_r$  vs  $\beta$  for a case of  $M=1.5$ ,  $m=0.1$ ,  $\Lambda=30^\circ$ ,  $\kappa=-2\kappa_L$ , and  $T_w=0.7$ . The star icons in (a) and (b) indicate  $\beta=0.2$  (black),  $1.0$  (red), and  $1.7$  (blue), and the green rhombus icons in (a) and (b) indicate the corresponding eigenmodes in (c). Dash line square in the inset of (b) denotes the regime for possible mode exchanges. (c) The corresponding disturbance profiles labeled by rhombus icons. The corresponding (d) streamwise velocity, (e) temperature, and (f) crossflow velocity disturbance profiles labeled by star icons. In (c)–(f), the dotted line represents the boundary layer edge.

The disturbance profiles of the two modes at  $\beta=1.136$  exhibit remarkable similarities [Fig. 13(c)], while the difference in  $\alpha_r$  being less than  $0.003\%$  [the inset of Fig. 13(b)]. As  $\beta$  increases, the crossflow disturbances slightly shift toward the boundary edge, while the peak disturbances consistently appear near the wall. Notably, a mode

exchange from the first GCF mode to the second GCF mode occurs after  $\beta=1.136$ . These findings suggest the presence of synchronization. The clustering of the disturbance near the wall may contribute to the thinner boundary layer thickness resulting from the cold wall condition.



Next, cases of  $M = 3.0$  are examined under changes in  $\Lambda$ ,  $\kappa$ , and  $T_w$ , as shown in Fig. 14. The first GCF mode is enhanced with a large  $\beta$  range at a small  $\Lambda$ , where the Görtler instability dominates. Further increasing  $\Lambda$  leads to two inflection points in the growth rate [identified in Fig. 14(a)], with  $\beta = 0.538$  considered as the synchronization regime at  $\Lambda = 10^\circ$ . When  $\Lambda > 20^\circ$ , only the first GCF mode is found to be unstable at  $\beta < 1$ . The increase in crossflow strength (increasing  $\Lambda$ ) leads to the decrease in  $\beta$  range for the most unstable mode. The peak growth rate for  $\Lambda = 1^\circ$  is at  $\beta = 0.75$ , while for  $\Lambda = 50^\circ$ , it is at  $\beta = 0.3$ . Similar to the case of  $M = 1.5$ , the introduction of  $\kappa$  destabilizes the instability, analogous to the curvature effect on the Görtler instability, covering larger  $\beta$  ranges. Cold wall temperature leads to the destabilization of the modes and the appearance of the mode exchange regime with two local maxima. Synchronization between the two GCF modes occurs at  $T_w = 0.5$ , and further decrease in  $T_w$  leads to the stabilization of first local maximum at around  $\beta = 0.8$  and the destabilization of second local maximum after an inflection point at around  $\beta = 1.3$ . Moreover, decrease in  $T_w$  leads to the shift of peak growth rate to larger  $\beta$  values.

The origins of the inflection points at  $\Lambda = 10^\circ$  and the corresponding eigenvalue spectrum and the disturbance profiles are presented in Fig. 15. The first inflection point, observed at approximately  $\beta = 0.65$  in Fig. 14(a), results from the synchronization between the first and second GCF modes at  $\beta = 0.538$ . The second inflection point emerges from the higher growth rate of the first GCF mode compared with the second GCF mode at  $\beta > 1.1$  when synchronization is absent. In other words, the first GCF mode dominates at  $\beta < 0.6$  and  $\beta > 1.1$ , while the second GCF mode is dominant within the range of  $0.6 < \beta < 1.1$ . As  $\Lambda$  increases further, the second GCF mode becomes stable across the entire  $\beta$  range. Evidence of synchronization is provided in Fig. 15(c), where the two disturbance profiles exhibit close similarities at  $\beta = 0.538$ . The inset of Fig. 15(b) indicates that the difference in  $\alpha_r$  values is around 0.015%, which is deemed sufficiently small. The profiles shown in Figs. 14(d)–14(f) reveal that as  $\beta$  increases, the disturbances shift toward the boundary layer edge for the first GCF mode, while for the second GCF mode, the disturbances shift toward the wall. In other words, the exchange of the most unstable mode is identified after the synchronization as  $\beta$  increases, i.e., from the first GCF mode to the second GCF mode.

The eigenvalues across  $\beta$  for  $T_w = 0.5$  in the  $M = 3.0$  case are shown in Figs. 16(a) and 16(b). Synchronization between the first and second GCF modes is observed at  $\beta = 0.766$ , supported by the close similarities between the two disturbance profiles [shown in Fig. 16(c)], while the difference in  $\alpha_r$  is less than 0.04% [shown in the inset of Fig. 16(b)]. Mode exchanges are evident, with the crossflow disturbances shifting toward the boundary layer edge for the first GCF mode, while for the second GCF mode, the disturbances shift toward the wall [Fig. 16(f)]. Regarding the temperature disturbance profile [i.e., Figs. 16(c) and 16(e)], two peaks are observed instead of one within the boundary layer for the first GCF mode, unlike the case at the adiabatic wall temperature [i.e., Figs. 15(c) and 15(e)] and the cold wall case at low Mach number (i.e., Fig. 13). For reference, a similar case with  $T_w = 1$  is presented in Fig. 17. Comparing the disturbance temperature profiles in Fig. 17(b), it is evident that the peak near the wall rises as the wall temperature decreases, while the opposite trend is observed for the peak near the boundary layer edge. This phenomenon of temperature disturbance redistribution under different wall temperatures has been reported in the literature as well, for instance, by Liang *et al.* (2010)<sup>39</sup> in the investigation of Mack modes. As previously mentioned, the wall cooling leads to a thinner boundary layer thickness and the destabilization of modal instabilities, i.e., Görtler instability. It is postulated that the occurrence of the synchronization is closely related to the destabilization of the modal instability, which is manifested by the increased temperature disturbance strength near the wall.

For the  $M = 4.5$  cases (shown in Fig. 18), the increase in  $\Lambda$  again leads to the stabilization of the GCF mode. However, unlike the lower Mach number cases, the first GCF mode is always dominant across  $\beta$  with no mode exchange regime. The peak growth rate for  $\Lambda = 1^\circ$  is at  $\beta = 0.5$ , while for  $\Lambda = 50^\circ$ , it is at  $\beta = 0.25$ . The closer proximity of these two peaks compared to the lower Mach number cases suggests that the shift of the first GCF peak growth rate across  $\beta$  is less sensitive to changes in  $\Lambda$ . The increase in concave curvature again leads to the destabilization of the flow with the expansion of the unstable  $\beta$  range, akin to the destabilization of Görtler instability by wall curvature. An inflection point with two peaks is observed under cold wall conditions with  $T_w = 0.1$  and  $T_w = 1$  [Fig. 18(c)], implying that a mode exchange may presents at the cold wall condition.

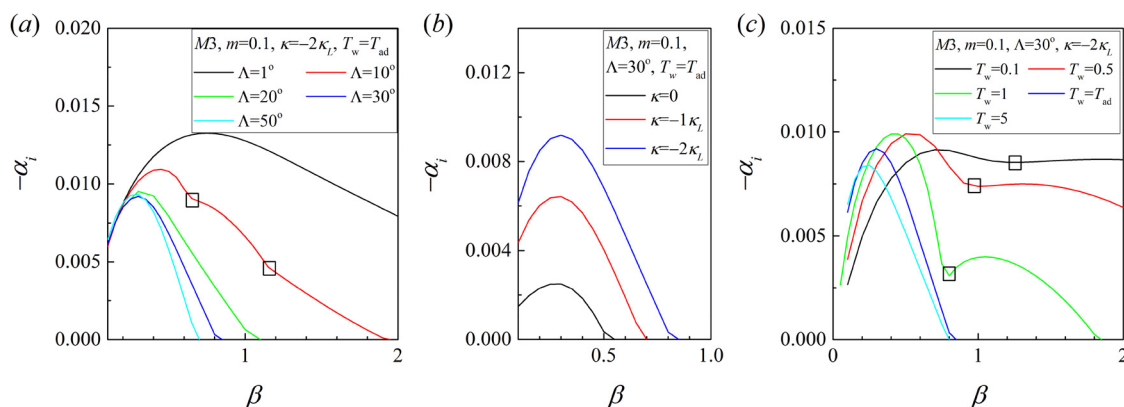


**FIG. 14.** Spatial maximum growth rate vs spanwise wavenumber at  $M = 3.0$  and  $\omega = 0$  with the change in (a) local sweep angle at  $m = 0.1$ ,  $\kappa = -2\kappa_L$ , and  $T_w = T_{ad}$ , (b) wall curvature at  $m = 0.1$ ,  $\Lambda = 30^\circ$ , and  $T_w = T_{ad}$ , and (c) wall temperature at  $m = 0.1$ ,  $\Lambda = 30^\circ$ , and  $\kappa = -2\kappa_L$ . Squares in (a) and (c) indicate the inflection points.

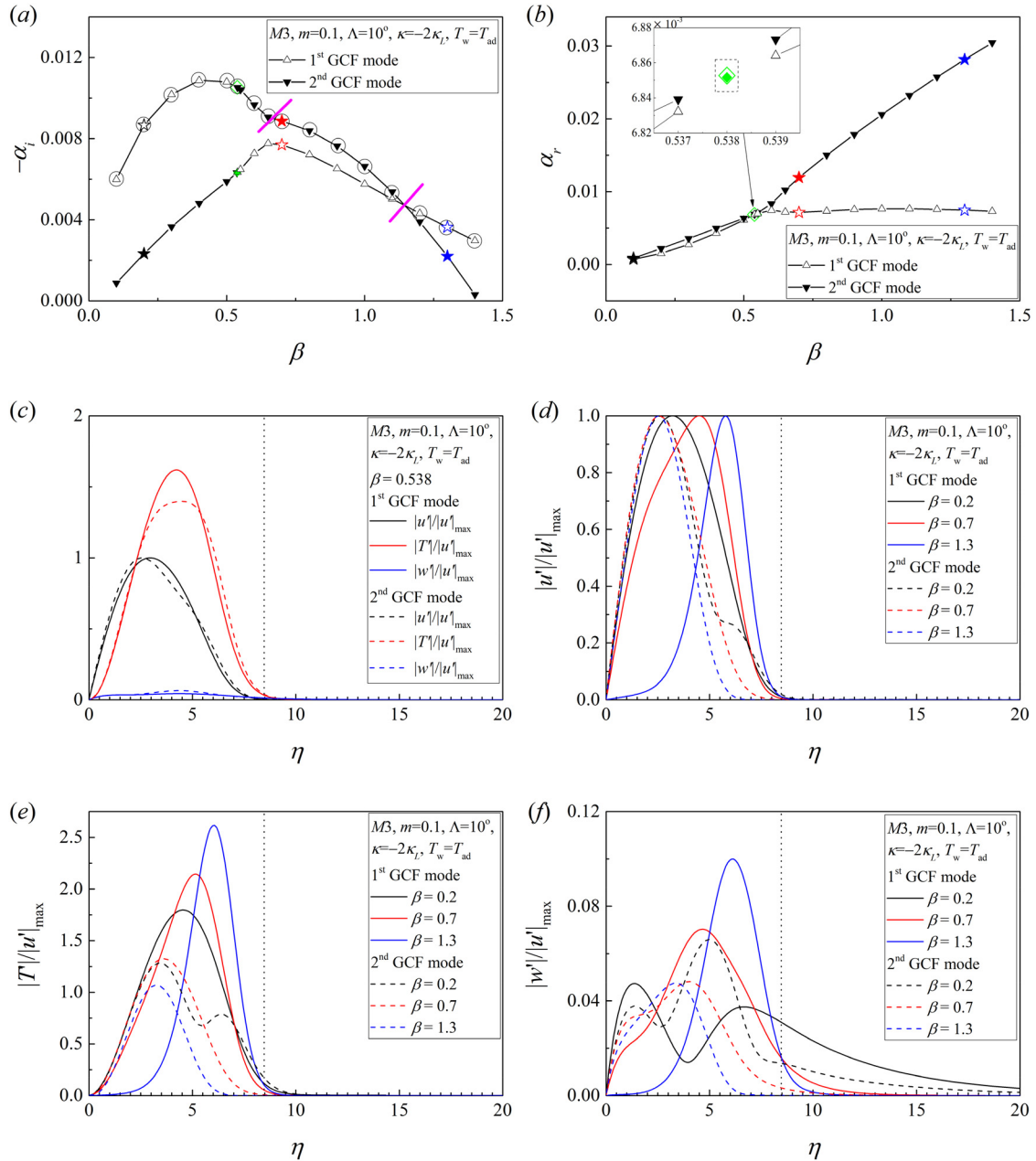


**FIG. 15.** (a) Growth rate vs  $\beta$  and (b)  $\alpha_r$  vs  $\beta$  for a case of  $M=3.0$ ,  $m=0.1$ ,  $\Lambda=10^\circ$ ,  $\kappa=-2\kappa_L$ , and  $T_w=T_{ad}$ . The star icons in (a) and (b) indicate  $\beta=0.2$  (black),  $0.7$  (red), and  $1.3$  (blue), and the green rhombus icons in (a) and (b) indicate the corresponding eigenmodes in (c). Solid Magenta lines in (a) represent the inflection points indicated in Fig. 14(a). Dash line square in the inset of (b) denotes the regime for possible mode exchanges. (c) The corresponding disturbance profiles labeled by rhombus icons. The corresponding (d) streamwise velocity, (e) temperature, and (f) crossflow velocity disturbance profiles labeled by star icons. In (c)–(f), the dotted line represents the boundary layer edge.

The eigenvalue spectrum vs  $\beta$  for  $T_w=0.1$  is shown in Fig. 19, and synchronization of the first and second GCF modes is identified by the close similarities between the two disturbance profiles at  $\beta=0.668$  [Fig. 19(c)] with a difference in  $\alpha_r$  at approximately  $0.04\%$  [inset of Fig. 19(b)]. Similar to the cold wall case at  $M=3.0$

[i.e., Figs. 16(c) and 16(e)], the temperature disturbance profile for the first GCF mode in Figs. 19(c) and 19(e) consists of two peaks, showing that the natures of the GCF modes are altered at the cold wall temperature while the flow is destabilized, and thus, synchronization between the first and second GCF modes becomes possible.

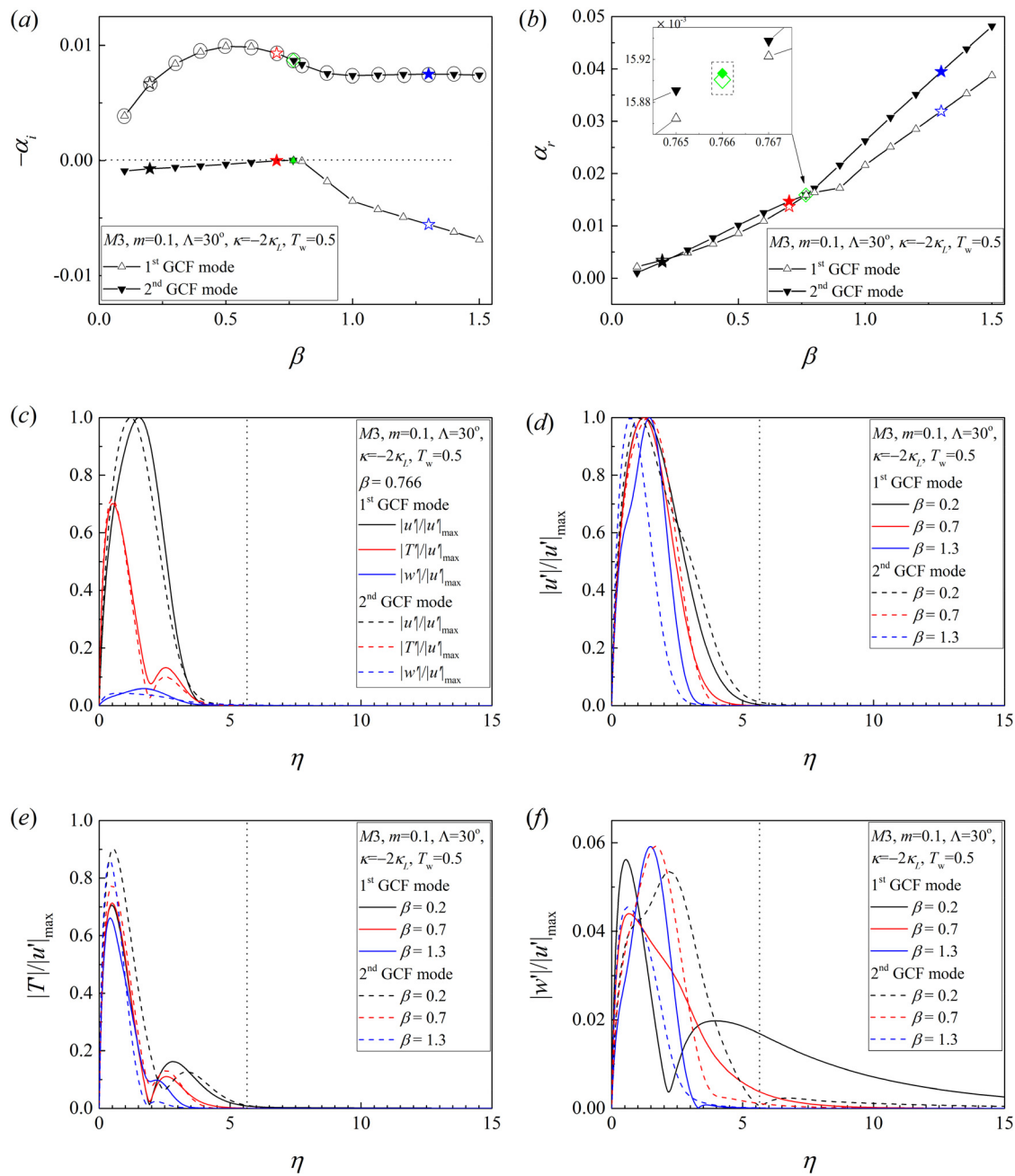


**FIG. 16.** (a) Growth rate vs  $\beta$  and (b)  $\alpha_r$  vs  $\beta$  for a case of  $M = 3.0$ ,  $m = 0.1$ ,  $\Lambda = 30^\circ$ ,  $\kappa = -2\kappa_L$ , and  $T_w = 0.5$ . The star icons in (a) and (b) indicate  $\beta = 0.2$  (black),  $0.7$  (red), and  $1.3$  (blue), and the green rhombus icons in (a) and (b) indicate the corresponding eigenmodes in (c). Dash line square in the inset of (b) denotes the regime for possible mode exchanges. (c) The corresponding disturbance profiles labeled by rhombus icons. The corresponding (d) streamwise velocity, (e) temperature, and (f) crossflow velocity disturbance profiles labeled by star icons. In (c)–(f), the dotted line represents the boundary layer edge.

To summarize, synchronization between the first and second GCF modes may occur under cold wall conditions or at a moderate sweep angle defined as the mode exchange regime in supersonic boundary layers. An unstable first GCF mode is always present, while the second GCF mode becomes more stable as the Mach

number increases. The shift of the peak growth rate for the first GCF mode across  $\beta$  becomes less sensitive to changes in  $\Lambda$  in the higher Mach number cases, indicating that both the most unstable Görtler and crossflow instability in high-speed boundary layers become indistinguishable. Notably, the synchronization regime

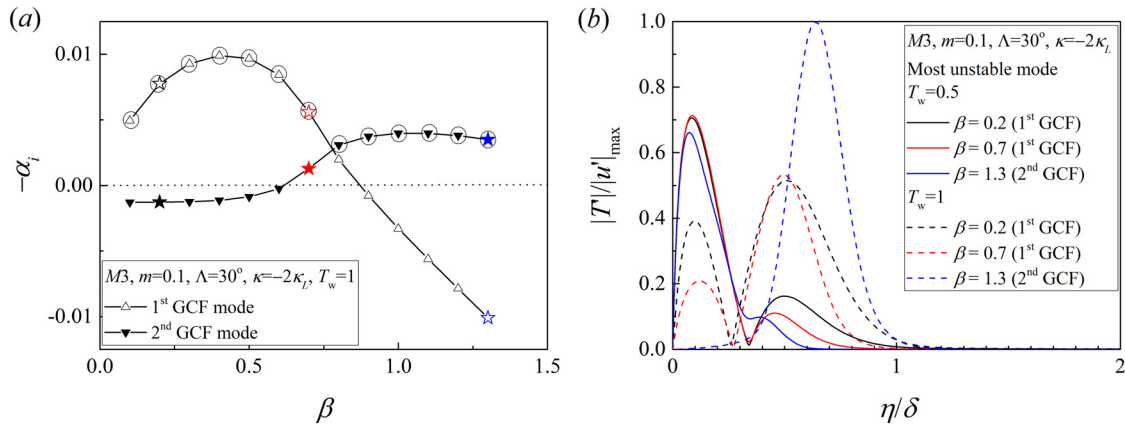


**FIG. 17.** (a) Growth rate vs  $\beta$  for a case of  $M=3.0$ ,  $m=0.1$ ,  $\Lambda=30^\circ$ ,  $\kappa=-2\kappa_L$ , and  $T_w=1.0$ . The star icons indicate  $\beta=0.2$  (black),  $0.7$  (red), and  $1.3$  (blue). (b) The corresponding temperature disturbance profiles for  $T_w=0.5$  [extracted from Fig. 16(e)] and  $T_w=1.0$  cases.  $\eta$  is scaled with  $\delta$ , where  $\delta$  denotes the  $\eta$  position at 99.9% of  $u_\theta$  for the specific flow conditions (i.e., boundary layer edge).

shifts to lower  $\Lambda$  values as Mach number increases (i.e., from  $\Lambda_{\text{syn}}=20^\circ$  at  $M=0.0001$  to  $\Lambda_{\text{syn}}=10^\circ$  at  $M=3.0$ , where  $\Lambda_{\text{syn}}$  denotes the sweep angle at which synchronization occurs). At  $M=4.5$ , only the features of multiple Görtler modes are retained with no synchronization, suggesting a weakened crossflow effect in competition with the Görtler modes in the supersonic regime. Analogous to the case of incompressible boundary layers, the disturbance moves away from the wall as  $\beta$  increases for the first GCF mode, while it is vice versa for the second GCF mode. Under the change of wall temperature, the synchronization regime shifts to the cold wall side as the Mach number increases (transitioning from  $T_w=0.7$  at  $M=1.5$  to  $T_w=0.1$  at  $M=4.5$ ). This implies that the destabilization of second GCF mode at cold wall conditions becomes more unattainable with increasing Mach numbers. This could be attributed to the increase in thermal effect at the synchronization regime as the Mach number increases. To illustrate, in the context of synchronization at a cold wall, the peak temperature disturbance near the wall is approximately 0.7 for  $M=3.0$

[as depicted in Fig. 16(c)], while the corresponding value is around 1.4 for  $M=4.5$  [as illustrated in Fig. 19(c)].

### C. Hypersonic boundary layers ( $M$ 6–10)

Finally, this subsection examines the GCF instability in hypersonic boundary layers. From  $M=6.0$  to  $10.0$  (shown in Figs. 20–22), the instability is stabilized at large  $\Lambda$ , destabilized at increased concave curvature and marginally destabilized at cold walls. Multiple unstable GCF modes are captured even at large  $\Lambda$  [i.e., multiple unstable modes are recorded for  $\Lambda=50^\circ$  in Figs. 20(a), 21(a), and 22(a), however, only the maximum growth rate is shown], unlike the incompressible/supersonic boundary layer cases. The presence of multiple unstable modes under different  $\Lambda$  resembles the characteristics of Görtler instability. This similarity suggests that hypersonic boundary layers with fixed curvature and swept angle are less sensitive to crossflow instability, while the characteristic of Görtler instability is mostly retained. Furthermore, synchronization between the first and second GCF

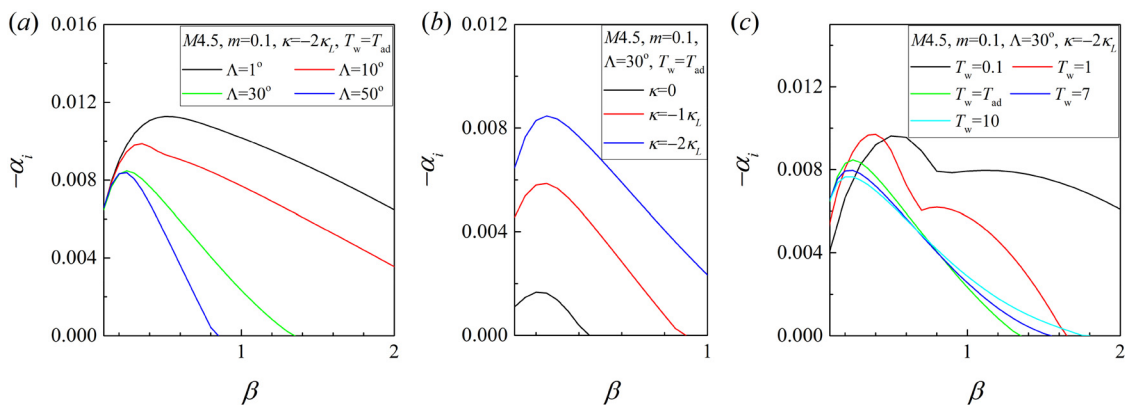


**FIG. 18.** Spatial maximum growth rate vs spanwise wavenumber at  $M=4.5$  and  $\omega=0$  with the change in (a) local sweep angle at  $m=0.1$ ,  $\kappa=-2\kappa_L$ , and  $T_w=T_{\text{ad}}$ , (b) wall curvature at  $m=0.1$ ,  $\Lambda=30^\circ$ , and  $T_w=T_{\text{ad}}$ , and (c) wall temperature at  $m=0.1$ ,  $\Lambda=30^\circ$ , and  $\kappa=-2\kappa_L$ .

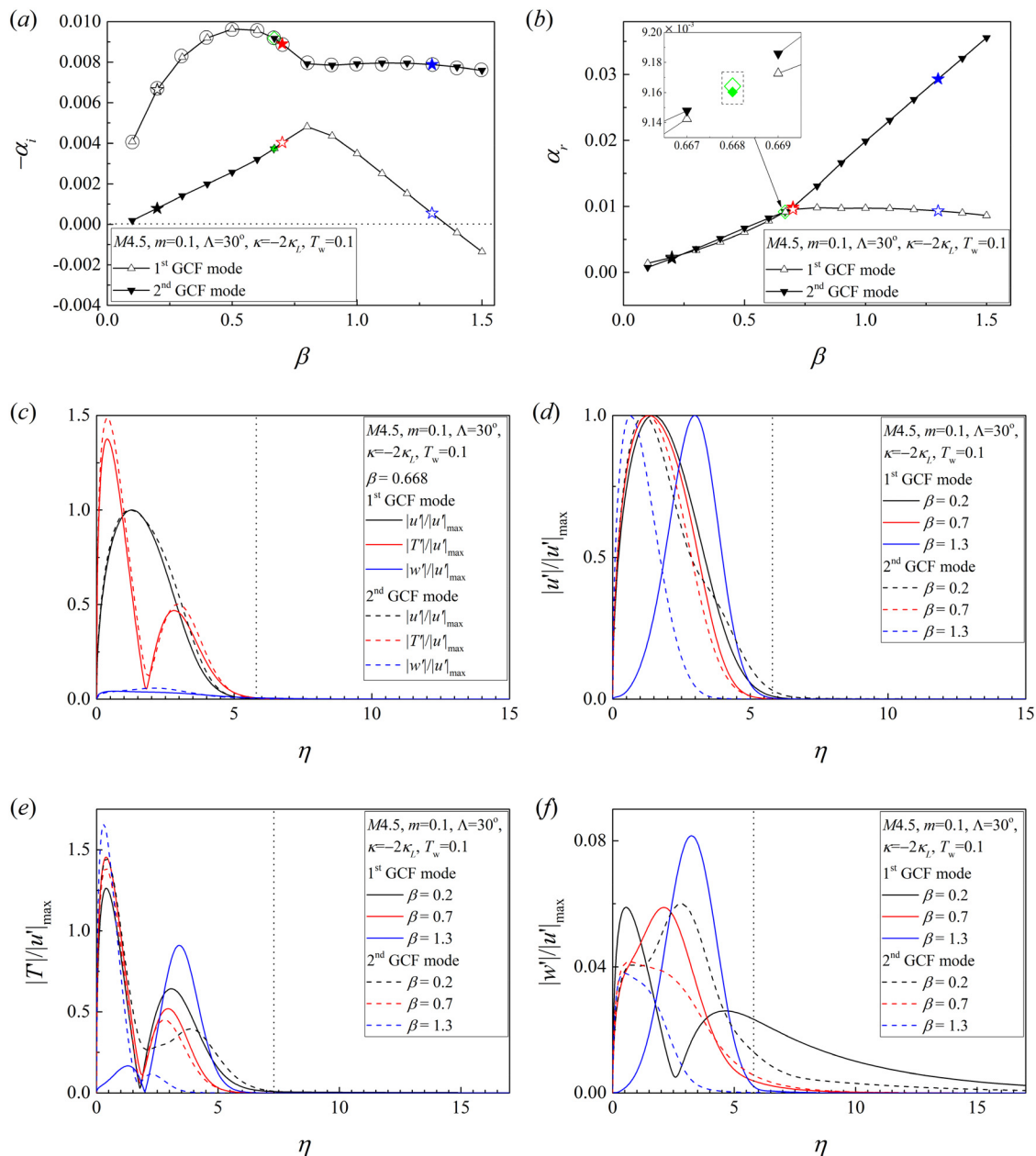


**FIG. 19.** Growth rate vs  $\beta$  and (b)  $\alpha_r$  vs  $\beta$  for a case of  $M=4.5$ ,  $m=0.1$ ,  $\Lambda=30^\circ$ ,  $\kappa=-2\kappa_L$ , and  $T_w=0.1$ . The star icons in (a) and (b) indicate  $\beta=0.2$  (black),  $0.7$  (red), and  $1.3$  (blue), and the green rhombus icons in (a) and (b) indicate the corresponding eigenmodes in (c). Dash line square in the inset of (b) denotes the regime for possible mode exchanges. (c) The corresponding disturbance profiles labeled by rhombus icons. The corresponding (d) streamwise velocity, (e) temperature, and (f) crossflow velocity disturbance profiles labeled by star icons. In (c)–(f), the dotted line represents the boundary layer edge.

modes is absent in these high Mach number regimes. The first GCF mode is always the dominant mode across  $\beta$ . The instability becomes much more unstable across larger  $\beta$  ranges if the role of concave curvature becomes dominant over the crossflow [i.e., in Figs. 20(b), 21(b), and 22(b), the crossflow mode with zero curvature is unstable at  $\beta < 0.4$ , while the unstable  $\beta$  ranges expands beyond  $\beta = 1$  once the

concave curvature is included]. The strength of the crossflow instability at zero curvature and a fixed sweep angle is relatively weak (i.e., maximum  $-\alpha_i \approx 0.001$ ) compared to the cases involving curvature (i.e., maximum  $-\alpha_i \approx 0.008$ ). This observation suggests that the impact of crossflow instability on hypersonic boundary layers is limited in comparison with the impact of Görtler instability.



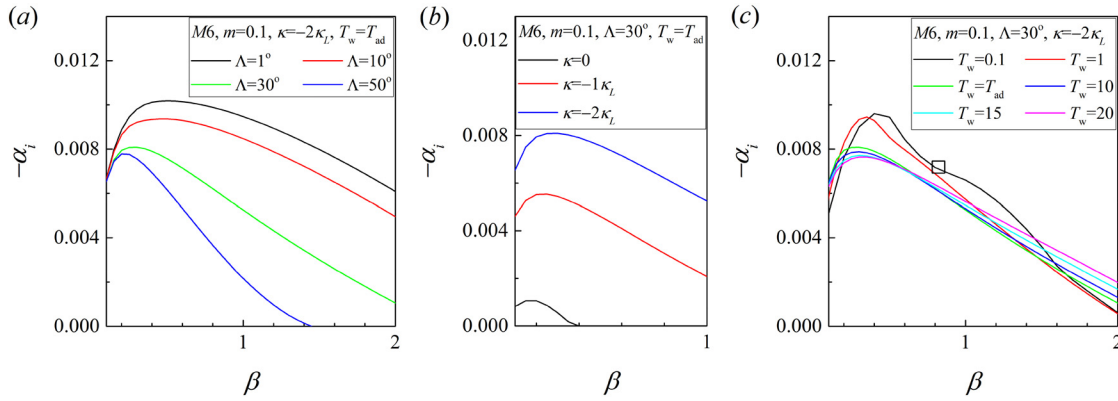


**FIG. 20.** Spatial maximum growth rate vs spanwise wavenumber at  $M=6.0$  and  $\omega=0$  with the change in (a) local sweep angle at  $m=0.1$ ,  $\kappa=-2\kappa_L$ , and  $T_w=T_{ad}$ , (b) wall curvature at  $m=0.1$ ,  $\Lambda=30^\circ$ , and  $T_w=T_{ad}$ , and (c) wall temperature at  $m=0.1$ ,  $\Lambda=30^\circ$ , and  $\kappa=-2\kappa_L$ . Square in (c) indicates the inflection point.

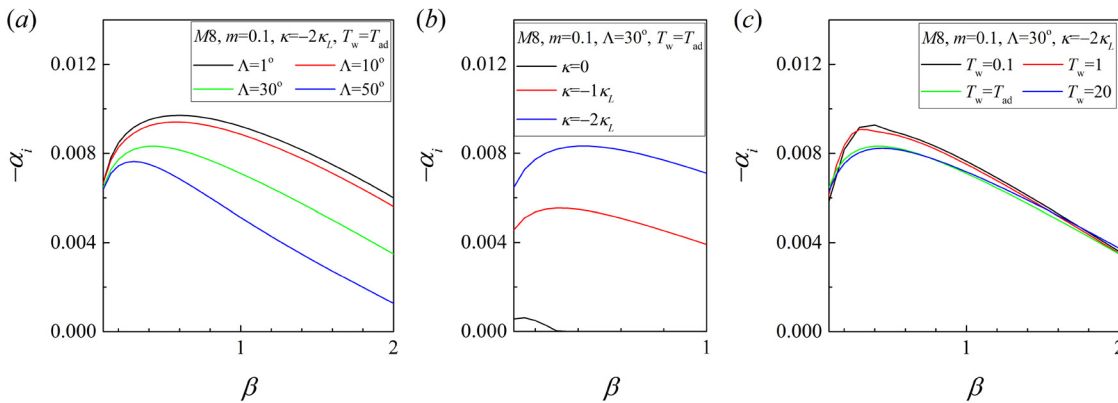


**FIG. 21.** Spatial maximum growth rate vs spanwise wavenumber at  $M=8.0$  and  $\omega=0$  with the change in (a) local sweep angle at  $m=0.1$ ,  $\kappa=-2\kappa_L$ , and  $T_w=T_{ad}$ , (b) wall curvature at  $m=0.1$ ,  $\Lambda=30^\circ$ , and  $T_w=T_{ad}$ , and (c) wall temperature at  $m=0.1$ ,  $\Lambda=30^\circ$ , and  $\kappa=-2\kappa_L$ .

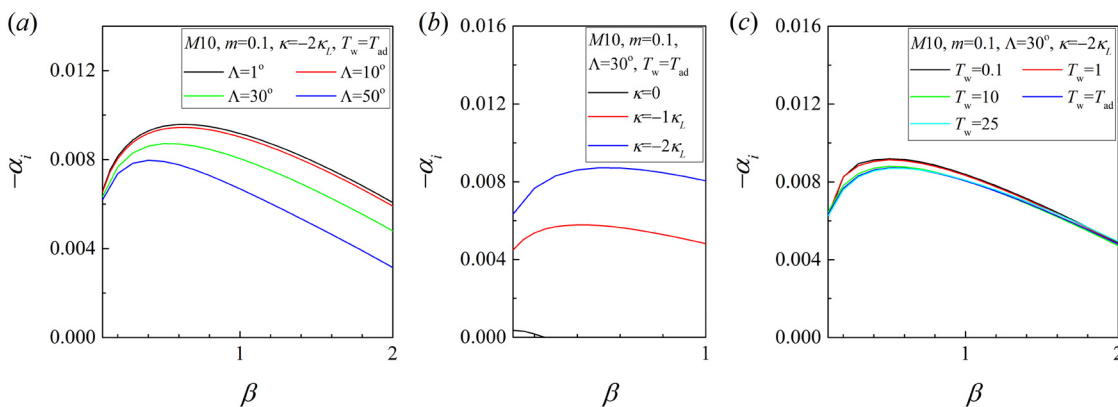


**FIG. 22.** Spatial maximum growth rate vs spanwise wavenumber at  $M=10.0$  and  $\omega=0$  with the change in (a) local sweep angle at  $m=0.1$ ,  $\kappa=-2\kappa_L$ , and  $T_w=T_{ad}$ , (b) wall curvature at  $m=0.1$ ,  $\Lambda=30^\circ$ , and  $T_w=T_{ad}$ , and (c) wall temperature at  $m=0.1$ ,  $\Lambda=30^\circ$ , and  $\kappa=-2\kappa_L$ .

Figures 20(c), 21(c), and 22(c) demonstrate that the extremely cold wall with  $T_w = 0.1$  destabilizes the peak GCF mode, while further increases in  $T_w$  over  $T_{ad}$  have an insignificant effect on the GCF instability. Notably, in the case of  $M = 6$  case with  $T_w = 0.1$  [as illustrated in Fig. 20(c)], an inflection point is observed. However, upon closer examination, the disturbance profiles near this point are found to be substantially different (not shown), indicating the absence of synchronization between the modes.

In conclusion, the Görtler instability is always dominant over the crossflow instability in hypersonic boundary layers. Thus, no synchronization is observed, and the characteristics of multiple Görtler modes are retained in the overall GCF instability. The crossflow instability can be considered as the extension of the Görtler instability from a 2D base flow to a 3D one at hypersonic regime, analogous to the concept given in Liu's work<sup>26</sup> on the effect of crossflow to the first Mack mode (or T-S mode) in such high Mach number regime.

#### IV. CONCLUSIONS

In this study, the coexistence of steady Görtler and crossflow instability covering the incompressible to hypersonic boundary layers was investigated by varying the local sweep angle, pressure gradient, wall curvature and wall temperature. Modal growth of the compressible FSC base flows was identified using the LST.

In incompressible boundary layers, increasing the local sweep angle under a fixed concave curvature leads to the appearance of two unstable modes near a certain sweep angle. These modes are conventionally regarded as the crossflow mode and the Görtler mode. Previous literature has suggested that a changeover between Görtler and crossflow instability occurs. However, this study shows that the corresponding disturbance profiles obtained differ from those of solely the crossflow or Görtler mode. Instead, the appearance of the two unstable modes at the changeover regime can be attributed to the synchronization of the two Görtler–crossflow (GCF) modes, which share characteristics similar to multiple Görtler modes. The definition of the changeover regime appears to be inappropriate. To avoid the ambiguity, the mode exchange regime is defined accordingly in which the most unstable mode exchanges from the first GCF mode to the second GCF mode after the synchronization. Three scenarios are presented to summarize the possible development of GCF instability:

- (1) When the Görtler instability dominates over the crossflow instability (i.e., at a fixed curvature and small local sweep angles), the first GCF mode is always unstable across a large spanwise wavenumber range. The second GCF mode is always more stable than the first GCF mode, analogous to the Görtler instability.
- (2) When both the crossflow and Görtler instabilities are important (i.e., at a fixed curvature, near the mode exchange sweep angle), synchronization between the first and second GCF modes occurs. The maximum growth rate of the unstable first GCF mode shifts to smaller spanwise wavenumbers, and the unstable second GCF mode arises after synchronization.
- (3) When the crossflow instability dominates over the Görtler instability (i.e., at a fixed curvature and large local sweep angles), the unstable first GCF mode has a local maximum within small spanwise wavenumber ranges. The second GCF mode is always stable, even after synchronization with the first GCF mode.

The effect of curvature destabilizes the instability, and the introduction of a pressure gradient stabilizes the instability, thus validating the findings in previous literature.

Supersonic boundary layer regimes with  $M = 1.5, 3.0$ , and  $4.5$  were tested with individual changes in the local sweep angle, wall curvature and wall temperature. Similar to incompressible boundary layers, increasing the local sweep angle at fixed curvature shifted the local maximum growth rate to smaller spanwise wavenumbers, and both increasing concave wall curvature and decreasing wall temperature destabilized the instability. Synchronization of the two GCF modes was observed under two conditions: (1) a change in local sweep angle at  $M = 1.5$  and  $3.0$  and (2) cold wall temperature at  $M = 1.5, 3.0$ , and  $4.5$ . The second GCF mode may become unstable after synchronization, analogous to the incompressible boundary layer cases. Shifts of synchronization regime to lower sweep angle and cold wall side are observed as Mach number increases. The former signifies a weakened crossflow compared with the Görtler instability with increasing Mach number, while the latter implies that the synchronization closely related to the thermal content in compressible flows.

Finally, the study investigated the hypersonic boundary layers at  $M = 6.0, 8.0$ , and  $10.0$ . The overall trend of destabilization under changes in the local sweep angle, wall curvature and wall temperature were found to be identical to the supersonic boundary layer cases. However, in the hypersonic boundary layers, the first GCF mode always played the dominant role across  $\beta$ , and no synchronization was observed. The crossflow instability has a limited impact on the overall GCF instability.

This study reveals that the instabilities resulting from the Görtler and crossflow effects exhibit behaviors akin to the multiple modes observed in the Görtler instability. Although these findings are based on local stability assumptions, they shed light on the genesis of such instabilities in boundary layers at various Mach number regimes. More interpretation on the GCF modes can be revealed through numerical simulations in the future. Subsequent investigations can delve into the intricacies of the coexistence of all three modal instabilities including the first Mack mode under the influence of traveling disturbances, allowing for a comprehensive exploration in the next step.

#### ACKNOWLEDGMENTS

This study was supported by the Hong Kong Research Grants Council (Nos. 15216621, 15206519, and 25203721) and the National Natural Science Foundation of China (No. 12102377).

#### AUTHOR DECLARATIONS

##### Conflict of Interest

The authors have no conflicts to disclose.

#### Author Contributions

**Ken Chun Kit Uy:** Conceptualization (equal); Data curation (equal); Formal analysis (equal); Investigation (equal); Methodology (equal); Software (equal); Validation (equal); Writing – original draft (equal); Writing – review & editing (equal). **Jiaao Hao:** Conceptualization (equal); Formal analysis (equal); Funding acquisition (equal); Investigation (equal); Project administration (equal);

Resources (equal); Supervision (equal); Writing – review & editing (equal). **Chih-Yung Wen:** Conceptualization (equal); Funding acquisition (equal); Project administration (equal); Resources (equal); Supervision (equal); Writing – review & editing (equal).

## DATA AVAILABILITY

The data that support the findings of this study are available from the corresponding author upon reasonable request.

## REFERENCES

- <sup>1</sup>G. Huang, X. Chen, J. Chen, X. Yuan, and G. Tu, “The stabilizing effect of grooves on Görtler instability-induced boundary layer transition in hypersonic flow,” *Phys. Fluids* **35**, 041701 (2023).
- <sup>2</sup>X. Li, Y. Zhang, H. Yu, Z.-K. Lin, H.-J. Tan, and S. Sun, “Görtler vortices behavior and prediction in dual-incident shock-wave/turbulent-boundary-layer interactions,” *Phys. Fluids* **34**, 106103 (2022).
- <sup>3</sup>H. Men, X. Li, and H. Liu, “Direct numerical simulations of hypersonic boundary layer transition over a hypersonic transition research vehicle model lifting body at different angles of attack,” *Phys. Fluids* **35**, 044111 (2023).
- <sup>4</sup>C. Thomas and S. Mughal, “Optimizing control of stationary cross-flow vortices excited by surface roughness,” *Phys. Fluids* **34**, 114104 (2022).
- <sup>5</sup>A. Srokowski and S. Orszag, *Mass Flow Requirements for LFC Wing Design* (American Institute of Aeronautics and Astronautics, 1977).
- <sup>6</sup>H. L. Reed and W. S. Saric, “Stability of three-dimensional boundary layers,” *Annu. Rev. Fluid Mech.* **21**, 235 (1989).
- <sup>7</sup>M. R. Malik and D. I. A. Poll, “Effect of curvature on three-dimensional boundary-layer stability,” *AIAA J.* **23**, 1362 (1985).
- <sup>8</sup>D. Tempelmann, A. Hanifi, and D. S. Henningson, “Spatial optimal growth in three-dimensional boundary layers,” *J. Fluid Mech.* **646**, 5 (2010).
- <sup>9</sup>W. S. Saric, H. L. Reed, and E. B. White, “Stability and transition of three-dimensional boundary layers,” *Annu. Rev. Fluid Mech.* **35**, 413 (2003).
- <sup>10</sup>H. L. Reed, “Wave interactions in swept-wing flows,” *Phys. Fluids* **30**, 3419 (1987).
- <sup>11</sup>Y. H. Zurigat and M. R. Malik, “Effect of cross-flow on Görtler instability in incompressible boundary layers,” *Phys. Fluids* **7**, 1616 (1995).
- <sup>12</sup>R. Kobayashi and H. Izumi, “Boundary-layer transition on a rotating cone in still fluid,” *J. Fluid Mech.* **127**, 353 (1983).
- <sup>13</sup>Y. Kohama, *Three-Dimensional Boundary Layer Transition on a Concave-Concave Curved Wall* (Springer, Berlin, Heidelberg, 1988).
- <sup>14</sup>H. Bippes, *Instabilities Developing in the Three-Dimensional Boundary Layer on Concave and Convex Curved Surfaces* (Springer, Berlin, Heidelberg, 1995).
- <sup>15</sup>P. Hall, “The Görtler vortex instability mechanism in three-dimensional boundary layers,” *Proc. R. Soc. London Ser. A* **399**, 135 (1985).
- <sup>16</sup>J. F. Collier and M. Malik, *Stationary Disturbances in Three-Dimensional Boundary Layers over Concave Surfaces* (American Institute of Aeronautics and Astronautics, 1987).
- <sup>17</sup>A. P. Bassom and P. Hall, “Vortex instabilities in three-dimensional boundary layers: The relationship between Görtler and crossflow vortices,” *J. Fluid Mech.* **232**, 647 (1991).
- <sup>18</sup>J. C. Cooke, “The boundary layer of a class of infinite yawed cylinders,” *Math. Proc. Cambridge Philos. Soc.* **46**, 645 (1950).
- <sup>19</sup>N. D. Blackaby and M. Choudhari, “Inviscid vortex motions in weakly three-dimensional boundary layers and their relation with instabilities in stratified shear flows,” *Proc. R. Soc. London Ser. A* **440**, 701 (1993).
- <sup>20</sup>N. Itoh, “Multiple instabilities of three-dimensional boundary layers along a concave wall,” *Fluid Dyn. Res.* **13**, 81 (1994).
- <sup>21</sup>S. Otto and J. Denier, “The effect of crossflow on Görtler vortices,” ICASE Report No. 94-19 (ICASE, 1994).
- <sup>22</sup>C. Le Cunff and A. Zebib, “Görtler-crossflow vortices,” *Phys. Fluids* **9**, 2519 (1997).
- <sup>23</sup>A. Bottaro and P. Luchini, “Görtler vortices: Are they amenable to local eigenvalue analysis?” *Eur. J. Mech. B* **18**, 47 (1999).
- <sup>24</sup>K. J. Groot, J. Patel, E. S. Beyak, J. G. Coder, and H. L. Reed, *Görtler Instability on a Variably Swept, Slotted, Natural-Laminar-Flow Airfoil* (American Institute of Aeronautics and Astronautics, 2021).
- <sup>25</sup>Z. Liu, “Compressible Falkner–Skan–Cooke boundary layer on a flat plate,” *Phys. Fluids* **33**, 126109 (2021).
- <sup>26</sup>Z. Liu, “Cross-flow linear instability in compressible boundary layers over a flat plate,” *Phys. Fluids* **34**, 094110 (2022).
- <sup>27</sup>Z. Liu, “On the identification of cross-flow mode in three-dimensional boundary layers,” *AIP Adv.* **13**, 015203 (2023).
- <sup>28</sup>Y. Ma and X. Zhong, “Receptivity of a supersonic boundary layer over a flat plate—Part I: Wave structures and interactions,” *J. Fluid Mech.* **488**, 31 (2003).
- <sup>29</sup>J. Ren and S. Fu, “Competition of the multiple Görtler modes in hypersonic boundary layer flows,” *Sci. China: Phys. Mech. Astron.* **57**, 1178 (2014).
- <sup>30</sup>R. Song, L. Zhao, and Z. Huang, “Secondary instability of stationary Görtler vortices originating from first/second Mack mode,” *Phys. Fluids* **32**, 034109 (2020).
- <sup>31</sup>G. Guennebaud, B. Jacob *et al.*, “Eigen v3” (2010), see [https://eigen.tuxfamily.org/index.php?title=Main\\_Page](https://eigen.tuxfamily.org/index.php?title=Main_Page).
- <sup>32</sup>M. R. Malik, “Numerical methods for hypersonic boundary layer stability,” *J. Comput. Phys.* **86**, 376 (1990).
- <sup>33</sup>K. C. K. Uy, J. Hao, and C.-Y. Wen, “Global and local analyses of the Görtler instability in hypersonic flow,” *Phys. Fluids* **35**, 064111 (2023).
- <sup>34</sup>J. Ren, *Secondary Instabilities of Görtler Vortices in High-Speed Boundary Layers: Mechanisms and Flow Control on Laminar-Turbulent Transition* (Springer, 2017).
- <sup>35</sup>J. M. Floryan, “The second mode of the Goertler instability of boundary layers,” *AIAA J.* **23**, 1828 (1985).
- <sup>36</sup>S. Unnikrishnan and D. V. Gaitonde, “Instabilities and transition in cooled wall hypersonic boundary layers,” *J. Fluid Mech.* **915**, A26 (2021).
- <sup>37</sup>R. E. Spall and M. R. Malik, “Goertler vortices in supersonic and hypersonic boundary layers,” *Phys. Fluids A* **1**, 1822 (1989).
- <sup>38</sup>D. Arnal, *Boundary Layer Transition: Predictions Based on Linear Theory* (1994).
- <sup>39</sup>X. Liang, X. Li, D. Fu, and Y. Ma, “Effects of wall temperature on boundary layer stability over a blunt cone at Mach 7.99,” *Comput. Fluids* **39**, 359 (2010).